

Galaxy And Mass Assembly (GAMA): *ugrizYJHK* Sérsic luminosity functions and the cosmic spectral energy distribution by Hubble type

Lee S. Kelvin,^{1,2,3} Simon P. Driver,^{2,3} Aaron S. G. Robotham,^{2,3}
 Alister W. Graham,⁴ Steven Phillipps,⁵ Nicola K. Agius,⁶ Mehmet Alpaslan,^{2,3}
 Ivan Baldry,⁷ Steven P. Bamford,⁸ Joss Bland-Hawthorn,⁹ Sarah Brough,¹⁰
 Michael J. I. Brown,¹¹ Matthew Colless,¹² Christopher J. Conselice,⁸
 Andrew M. Hopkins,¹⁰ Jochen Liske,¹³ Jon Loveday,¹⁴ Peder Norberg,¹⁵
 Kevin A. Pimbblet,^{11,16,17} Cristina C. Popescu,⁶ Matthew Prescott,¹⁸
 Edward N. Taylor,¹⁹ and Richard J. Tuffs²⁰

¹*Institut für Astro- und Teilchenphysik, Universität Innsbruck, Technikerstraße 25, 6020 Innsbruck, Austria*

²*School of Physics and Astronomy, University of St Andrews, North Haugh, St Andrews, Fife, KY16 9SS, UK*

³*International Centre for Radio Astronomy Research, 7 Fairway, The University of Western Australia, Crawley, Perth, Western Australia 6009, Australia*

⁴*Centre for Astrophysics and Supercomputing, Swinburne University of Technology, Hawthorn, Victoria 3122, Australia*

⁵*Astrophysics Group, H.H. Wills Physics Laboratory, University of Bristol, Tyndall Avenue, Bristol BS8 1TL, UK*

⁶*Jeremiah Horrocks Institute, University of Central Lancashire, Preston PR1 2HE, UK*

⁷*Astrophysics Research Institute, Liverpool John Moores University, Twelve Quays House, Egerton Wharf, Birkenhead CH41 1LD, UK*

⁸*School of Physics and Astronomy, The University of Nottingham, University Park, Nottingham, NG7 2RD, UK*

⁹*Sydney Institute for Astronomy, School of Physics A28, University of Sydney, NSW 2006, Australia*

¹⁰*Australian Astronomical Observatory, PO Box 915, North Ryde, NSW 1670, Australia*

¹¹*School of Physics, Monash University, Clayton, VIC 3800, Australia*

¹²*Research School of Astronomy and Astrophysics, The Australian National University, Canberra, ACT 2611, Australia*

¹³*European Southern Observatory, Karl-Schwarzschild-Str. 2, 85748 Garching, Germany*

¹⁴*Astronomy Centre, University of Sussex, Falmer, Brighton BN1 9QH, UK*

¹⁵*Institute for Computational Cosmology, Department of Physics, Durham University, South Road, Durham DH1 3LE, UK*

¹⁶*Department of Physics, University of Oxford, Denys Wilkinson Building, Keble Road, Oxford OX1 3RH, UK*

¹⁷*Department of Physics and Mathematics, University of Hull, Cottingham Road, Hull, HU6 7RX, UK*

¹⁸*Astrophysics Group, Department of Physics, University of the Western Cape, 7535 Bellville, Cape Town, South Africa*

¹⁹*School of Physics, the University of Melbourne, Parkville, VIC 3010, Australia*

²⁰*Max Planck Institut für Kernphysik, Saupfercheckweg 1, D-69117 Heidelberg, Germany*

Draft

ABSTRACT

We report the morphological classification of 3727 galaxies from the Galaxy and Mass Assembly survey with $M_r < -17.4$ mag and in the redshift range $0.025 < z < 0.06$ (2.1×10^5 Mpc³) into E, S0-Sa, SB0-SBa, Sab-Scd, SBab-SBcd, Sd-Irr and little blue spheroid classes. Approximately 70% of galaxies in our sample are disk dominated systems, with the remaining $\sim 30\%$ spheroid dominated. We establish the robustness of our classifications, and use them to derive morphological-type luminosity functions and luminosity densities in the *ugrizYJHK* passbands, improving on prior studies that split by global colour or light profile shape alone. We find that the total galaxy luminosity function is best described by a double-Schechter function while the constituent morphological-type luminosity functions are well described by a single-Schechter function.

These data are also used to derive the star-formation rate densities for each Hubble class, and the attenuated and unattenuated (corrected for dust) cosmic spectral energy distributions, i.e., the instantaneous energy production budget. While the observed optical/near-IR energy budget is dominated 58:42 by galaxies with a significant spheroidal component, the actual energy production rate is reversed, i.e., the combined disk dominated populations generate $\sim 1.3\times$ as much energy as the spheroid dominated populations. On the grandest scale, this implies that chemical evolution in the local Universe is currently confined to mid-type spiral classes like our Milky Way.

Key words: galaxies: luminosity function, mass function – galaxies: fundamental parameters – galaxies: elliptical and lenticular, cD – galaxies: spiral

1 INTRODUCTION

In his seminal 1926 paper ‘Extra-galactic Nebulae’, Edwin Hubble established a framework for the morphological classification of galaxies which remains in use essentially unchanged to the present day. From a sample of 400 galaxies, and perhaps drawing inspiration from Jeans (1919) and Reynolds (1920), Hubble defined three main sub-groups; Elliptical, Spiral and Lenticular (Hubble 1926, 1936). Elliptical early-type galaxies typically show no additional structure beyond a smooth radial light profile. Conversely, late-type spiral galaxies consist of a central spheroidal bulge surrounded by a flattened extended disk containing spiral arm features, and perhaps with the presence of a bar. Lenticular galaxies fall somewhere in-between, with the familiar late-type bulge and disk features present, potentially with the addition of a bar, and yet the noticeable absence of spiral arm structure.

Many additions have been suggested to Hubble’s classification scheme, in order to account for, e.g.: the presence of rings (Sandage 1961); transition lenticular galaxies (Holmberg 1958); bulge-less Sd-type disk galaxies (Shapley & Paraskevopoulos 1940); the ‘boxy’ and ‘disky’ isophotes of early-type galaxies (Carter 1978; Davies et al. 1983; Carter 1987; Kormendy & Bender 1996); the large variation in lenticular bulge-to-disk ratios van den Bergh (1976); Laurikainen et al. (2010); Cappellari et al. (2011); Kormendy & Bender (2012), and; the presence of dwarf galaxies (Shapley 1938; Sandage & Binggeli 1984). These additions each provide important information to morphological classification schema, adding additional resolution to each classification element.

Moreover, while morphology is intrinsically linked to the star formation rate of the galaxy, it was shown by Dressler (1980) that the distribution of morphological types varies as a function of local galaxy density: the morphology-density relation. Many possible explanations for this exist in the literature, including four key effects: strangulation (Larson et al. 1980; Kauffmann et al. 1993; Diaferio et al. 2001), harassment (Moore et al. 1996), ram pressure stripping (Gunn & Gott 1972) and minor-merging or tidal interactions (Park et al. 2008). Each of these mechanisms in some way affects the star formation rate of the interacting system, shutting off star formation for galaxies in over-dense regions and consequently causing a change in colour and ultimately morphology. Possibly more fundamental than the relation between morphology and environment is the connection between galaxy structure (i.e.; bulge, disk, bar) and its host galaxy’s stellar mass (van der Wel 2008; Bamford et al. 2009; Nair & Abraham 2010; Wilman & Erwin 2012; Pimblet & Jensen 2012).

The logical basis for defining these morphological groupings remains a visual one, and so becomes increasingly time consuming in an era of large scale observational astronomy. Despite this, the scientific worth of morphological classification remains extremely high. The morphological class of a galaxy is a tracer of its evolutionary history, with merging events believed to be the primary cause of the transition of late-type spirals into early-type ellipticals (e.g., Park et al. 2008).

In this paper we provide morphological classifications for a local ($0.025 < z < 0.06$) volume limited sample of 3, 727

galaxies brighter than $M_{r,\text{Sérsic}} = -17.4$ mag taken from the Galaxy and Mass Assembly survey (GAMA; Driver et al. 2009). Using these classifications, we measure the global and constituent morphological-type luminosity functions in optical *ugriz*¹ and near-infrared *YJHK*² passbands.

This paper is structured as follows. We define our sample and postage stamp cutout creation in Section 2. This sample is morphologically classified by eye by three independent observers, described in Section 3. We explore the trends with morphology against complementary global galaxy measurements such as colour, stellar mass and Sérsic index in Section 4. We present the global and the individual morphological-type luminosity functions for all nine passbands in Section 5, and discuss the division of the cosmic spectral energy distribution by morphology, both with and without suitable corrections to account for dust attenuation, in Section 6. A standard cosmology of $(H_0, \Omega_m, \Omega_\Lambda) = (70 \text{ km s}^{-1} \text{ Mpc}^{-1}, 0.3, 0.7)$ is assumed throughout this paper.

2 DATA

Our data are taken from the GAMA survey (Driver et al. 2009, 2011), specifically GAMA phase 1, known as GAMA-I. GAMA is a combined spectroscopic and multi-wavelength imaging programme designed to study spatial structure in the nearby ($z < 0.25$) Universe on kpc to Mpc scales (see Driver et al. 2009 for an overview). The survey, after completion of phase 1, consists of three regions of sky each of 4 deg (Dec) \times 12 deg (RA), close to the equatorial region, at approximately 9^h (135 deg; G09), 12^h (180 deg; G12) and 14.5^h (217.5 deg; G15). The three regions were selected to enable accurate characterisation of the large scale structure over a range of redshifts and with regard to practical observing considerations and constraints. They lie within areas of sky surveyed by both the Sloan Digital Sky Survey (SDSS; York et al. 2000; Abazajian et al. 2009) as part of its Main Survey, and by the United Kingdom Infrared Telescope (UKIRT) as part of the UKIRT Infrared Deep Sky Survey (UKIDSS) Large Area Survey (UKIDSS-LAS; Lawrence et al. 2007). These data provide moderate depth and resolution imaging in *ugrizYJHK* suitable for analysis of nearby galaxies. GAMA imaging data presented in this paper is constructed from reprocessed SDSS and UKIDSS-LAS imaging data, rescaled to a common pixel scale of $0.339''/\text{pixel}$ and to a common zero point magnitude of 30 mag arcsec⁻². Further details on the GAMA imaging pipeline may be found in Hill et al. (2011). The accompanying spectroscopic input catalogue was derived from the SDSS PHOTO parameter (Stoughton et al. 2002) as described in Baldry et al. (2010). The GAMA spectroscopic programme (Robotham et al. 2010) commenced in 2008 using 2dF+AAOmega on the Anglo-Australian Telescope to obtain distance information (redshifts) for all galaxies brighter than $r < 19.8$ mag. The survey is ~ 99 per cent complete to $r < 19.4$ mag in G09 and G15 and $r < 19.8$ mag in G12, with a median redshift of $z \sim 0.2$. Full details of the GAMA Phase I (GAMA-I)

¹ These passbands have effective wavelength midpoints of 354, 475, 622, 763 and 905 nm, respectively.

² These passbands have effective wavelength midpoints of 1031, 1248, 1631 and 2201 nm, respectively.

spectroscopic programme, key survey diagnostics, and the GAMA public and team databases are given in Driver et al. (2011) and Hopkins et al. (2013).

2.1 Luminosity Limits

2.1.1 Absolute Sérsic Magnitudes

Although the GAMA survey limits mentioned above are defined using SDSS Petrosian photometry, our preferred measure of total magnitudes are those derived from truncated single-Sérsic fits to the data (see Kelvin et al. 2012). Initially a generalisation of the de Vaucouleurs (1948) $r^{1/4}$ model for describing the radial light profiles of early-type galaxies, the Sérsic (1963, 1968) $r^{1/n}$ model, subsequently reviewed in Graham & Driver (2005), has become a standard tool for quantifying galaxies across a wide range of morphologies, both early- and late-type. The Sérsic equation provides the intensity I at a given radius r as given by

$$I(r) = I_e \exp \left[-b_n \left(\left(\frac{r}{r_e} \right)^{1/n} - 1 \right) \right] \quad (1)$$

where I_e is the intensity at the effective radius r_e , the radius containing half of the projected total light, and n is the Sérsic index which determines the shape of the light profile. The value of b_n is a function of Sérsic index, as defined in Ciotti (1991), and is such that $\Gamma(2n) = 2\gamma(2n, b_n)$, where Γ and γ represent the complete and incomplete gamma functions respectively³. Single-Sérsic model fits have been shown to provide a good description of galaxy light profiles as faint as $B \sim 28$ mag/arcsec² (Caon et al. 1990, 1993, 1994). Therefore, Sérsic modelling allows for us to account for the missing flux in the wings of high central-concentration galaxies, side-stepping the well documented problems with both Petrosian and Kron photometry (see, e.g., Graham & Driver 2005; Graham et al. 2005). We elect to truncate our Sérsic magnitudes at 10 multiples of the half-light radius ($10 r_e$). This is to avoid extrapolation of flux into regimes below the limiting isophote for which we are uncertain of the true light profile of the galaxy: consequently not parametrising our ignorance. For further discussion of Sérsic photometry and truncation, see Kelvin et al. (2012).

For a given band x , absolute Sérsic magnitudes M_x are derived using the standard relation

$$M_x = m_x - (5 \log_{10} D_L + 25) - k_x - e_x - A_x \quad (2)$$

where m_x denotes the apparent magnitude (in this case, truncated Sérsic), D_L is the luminosity distance of the galaxy in megaparsecs (where D_L is related to the angular diameter distance, D_A , using the relation $D_L = (1+z)^2 D_A$), k_x is the applied k -correction for band x , e_x is the evolutionary correction and A_x is the Milky Way dust attenuation correction. We obtain appropriate k -corrections from version 8 of the GAMA-I stellar masses catalogue (*StellarMassesv08*; see Taylor et al. 2011). One would expect minimal evolutionary effects over the narrow redshift range of this sample

³ b_n can trivially be calculated using the programming language R using the relation $b_n = \text{qgamma}(0.5, 2n)$, where qgamma is the quantile function for the Gamma distribution. For the range $0.5 < n < 10$, Capaccioli (1989) approximates the value of b_n using the relation $b_n = 1.9992n - 0.3271$.

(see, e.g., Prescott et al. 2009), and so we do not apply any e -corrections to these data. We apply the Milky Way dust attenuation correction as given in Table 22 of Stoughton et al. (2002), with UKIDSS values determined by matching UKIDSS database values from the WFCAM Science Archive to the SDSS extinction in the r band. Further details on this procedure may be found in Liske et al. (in prep.).

2.1.2 Absolute Sérsic Magnitude Limit in the r Band

In order to avoid the many incompleteness issues affecting the dwarf systems (both Malmquist and surface-brightness bias), in this study we focus on the more luminous systems by removing those galaxies with an absolute Sérsic magnitude in the r band fainter than $M_r = -17.4$ mag. This value is determined based on the faintest magnitude down to which our GAMA sample would be complete at our upper redshift limit of $z = 0.06$ ($m_r \sim 19.4$ mag; see Appendix A and Figure 1). Sérsic and structural measurements are taken from version 7 of the GAMA-I Sérsic photometry catalogue (*SersicPhotometryv07*; Kelvin et al. 2012). To summarise this study; a 2-dimensional single-Sérsic model is fit to each galaxy in our sample using the SIGMA galaxy fitting pipeline. SIGMA is a wrapper around several contemporary commonplace astronomy tools including Source Extractor (Bertin & Arnouts 1996), PSF Extractor (Bertin 2011) and GALFIT (Peng et al. 2010).

2.2 Sample Definition

Using the latest version (version 16) of the GAMA-I tiling catalogue⁴ (*TilingCatv16*, see Baldry et al. 2010) we define a volume limited sample of 3,727 galaxy-like (*SURVEY_CLASS* ≥ 2) objects whose local flow-corrected redshifts z lie in the range $0.025 < z < 0.06$ (see Appendix A) with an associated normalised redshift quality $nQ > 2$ (i.e., good for science⁵), an extinction corrected r band SDSS Petrosian magnitude of $r < 19.4$ mag (ensuring a consistent depth across all three GAMA regions) and an absolute truncated Sérsic magnitude in the r -band of $M_r < -17.4$ mag. This luminosity and volume-limited sample of 3,727 galaxies is referred to as GAMA_{near}.

Our redshift limits give this sample a volume of 2.1×10^5 Mpc³. Note that redshifts have been matched from version 7 of the local flow corrected redshift catalogue (*DistancesFramesv07*), itself based on data from version 8 of the GAMA-I spectroscopic catalogue (*SpecObjv08*). These redshifts are Milky Way centric, but local velocity field effects have been removed. Matching to the GAMA galaxy group catalogue (G3C; Robotham et al. 2011), we find that just under half (1797, $\sim 48\%$) of our galaxies lie in identified groups with two or more members, with 672 galaxies

⁴ All GAMA catalogues are available through the GAMA database, available online at <http://www.gama-survey.org/>.

⁵ GAMA spectroscopic redshifts are assigned a quality from 0 to 4, where 0 is a corrupted/bad spectrum and therefore a meaningless associated redshift, and 4 is a high-quality redshift with a high degree of certainty. Typically, we advocate using $Q > 2$ for scientific analyses.

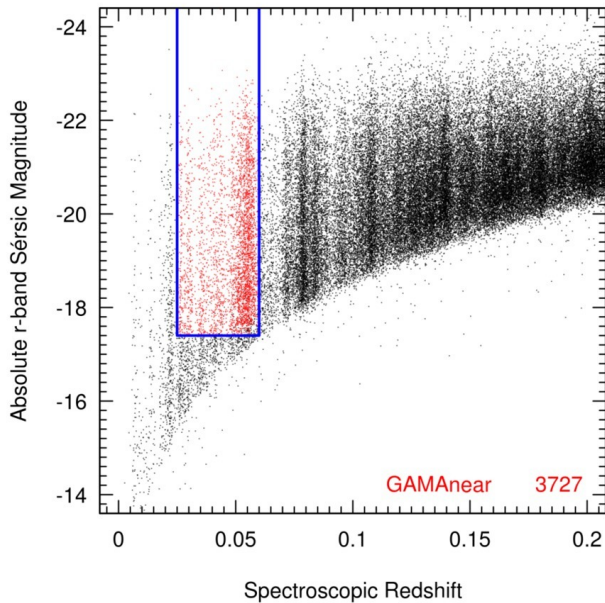


Figure 1. Absolute Sérsic magnitude (r band) as a function of local flow corrected spectroscopic redshift for galaxies within the GAMA survey. Red data points inside the blue box represent the 3,727 galaxies in the GAMAnear sample. Local flow-corrected spectroscopic redshifts are taken from version 7 of the local flow corrected redshift catalogue (*DistancesFramesv07*), and absolute Sérsic magnitudes from version 7 of the Sérsic photometry catalogue (*SersicCatAllv07*; Kelvin et al. 2012).

($\sim 18\%$) in groups with a richness greater than 5, i.e.; our sample is predominantly field dominated.

Figure 1 shows absolute Sérsic magnitude (r band) as a function of local flow corrected spectroscopic redshift for the full GAMA dataset (black points). Red data points inside the blue box represent the 3,727 galaxies in the GAMAnear sample. A summary of all GAMA data products used to define these samples are shown in Table 1.

2.3 Magnitude Limits in Additional Passbands

The r band absolute magnitude limit for our volume limited GAMAnear sample ($M_r = -17.4$ mag) introduces a colour-dependent limit across the remaining eight passbands in use from the SDSS and UKIDSS. This variable limit has the potential to introduce incompleteness bias when analysing data at other wavelengths, and so (following Driver et al. 2012), we define additional limits down to which the sample remains complete and unbiased as a function of colour for each passband.

The colour-magnitude diagrams in Figure 2 show the relation between colour and absolute magnitude for galaxies in the GAMAnear sample. Long dashed lines represent the r band limit of $M_r = -17.4$ mag. One can clearly see the two distinct populations (i.e., a bimodal distribution in both colour and absolute magnitude) in the g band data; the blue cloud and red sequence. These two populations are also evident to a lesser extent at all wavelengths.

We define the additional faint-end limits visually as the absolute magnitude in band x (where $x = ugizYJHK$) at

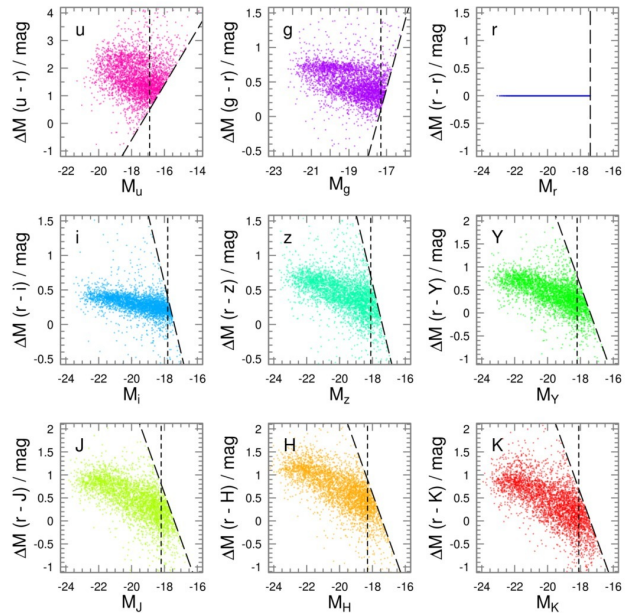


Figure 2. Colour-Magnitude diagrams for all galaxies in the GAMAnear sample across all nine bands. These values are derived from absolute Sérsic magnitudes truncated at $10 r_e$ with k -corrections and Galactic dust corrections applied. Long-dashed lines represent the volume-limited sample limit of $M_r = -17.4$ mag. Short-dashed lines represent the absolute magnitude at which the main body of data intersects the long-dashed line, and shows to what magnitude limit this sample is complete down to for that wavelength. These limits are listed in Table 2.

which the main body of the data intersects the $M_r = -17.4$ mag line. These passband limits are listed in Table 2, and shown as vertical short dashed lines in Figure 2. The absolute magnitude of the Sun in all passbands is also shown in Table 2, for reference (values taken from Table 1, Hill et al. 2010).

3 VISUAL CLASSIFICATION

3.1 Classification Criteria

Perhaps the most simplistic and robust means by which a sample of galaxies may be classified into their appropriate morphological types is by visual ‘eyeball’ inspection. We create three-colour postage stamp images for each galaxy in our GAMAnear sample of 3727 objects using the PI plotting tool, an internal GAMA software product⁶. For our analysis, we opt to take red, green and blue colours from the UKIDSS H and SDSS i and g bands, respectively.

Eyeball classification occurs in two phases. Phase 1 postage stamps depict $20'' \times 20''$ with the dynamic range of the images scaled logarithmically and prior decisions made on the lower (black) and upper (white) cut levels. Phase 2 postage stamps depict a larger area of $40'' \times 40''$ and are scaled using the arctan function. We found that the arctan function removes the necessity for a harsh upper or lower

⁶ A web version of this tool exists at the following web address: <http://thuban4.st-and.ac.uk/gama/colcutout/gamacutout.php>

DMU	Version	Catalogue	Paper	Summary of data products used in this study
InputCat	16	TilingCat	Baldry et al. (2010)	Target information (RA, Dec, SDSS Petrosian magnitude, Survey Class)
InputCat	16	InputCatA	Baldry et al. (2010)	Extinction corrections
LocalFlowCorrection	7	DistancesFrames	Baldry et al. (2012)	Local flow-corrected spectroscopic redshifts, redshift quality flags
StellarMasses	8	StellarMasses	Taylor et al. (2011)	Global galaxy colours, k -corrections (priv. comm.)
SersicPhotometry	7	SersicCatAll	Kelvin et al. (2012)	Sérsic photometry, Structural measurements

Table 1. A summary of the GAMA data products that have been collated for this study. GAMA catalogues and their associated data products are grouped into Data Management Units (DMUs), which are also listed here for reference.

Band	u	g	r	i	z	Y	J	H	K
Limit	−16.9	−17.3	−17.4	−17.8	−18.1	−18.2	−18.2	−18.3	−18.1
Number of galaxies below limit	2841	3445	3727	3536	3342	3195	3196	3236	3197
M_{\odot}	6.38	5.15	4.71	4.56	4.54	4.52	4.57	4.71	5.19

Table 2. Absolute Sérsic magnitude limits, galaxy number counts and absolute solar magnitudes. Sérsic limits denote the faint-end absolute magnitude at which the sample is complete for that band. Limits are defined as the absolute magnitude at which the main body of data in the colour-magnitude diagrams of Figure 2 intersect the volume-limited sample faint-end limit of $M_r = -17.4$. The number of galaxies refers to the how many galaxies from the GAMAnear sample are brighter than the limit in that band. The absolute magnitude of the Sun in all passbands is also shown, for reference.

cut level. Imposing harsh cuts has the potential to lead to misclassification as it imposes an apparent physical boundary in the light profile of a galaxy where none exists. The increased area of the phase 2 postage stamps also allows for the galaxy to be put into context of its local environment, and allows the observer to see more than the core of nearby extended galaxies.

Classification occurs by assigning the postage stamp of a galaxy into a specific directory hierarchy. A schematic representation of this hierarchy is shown in Figure 3, with final ‘master’ number counts inset for later reference. Postage stamp images are populated at the top level, and visual classification decisions eventually filter a galaxy down through this classification tree into its appropriate morphological class, from E to Sd-Irr, as indicated. The decision tree is essentially binary at each level (with the exception of stars and the ‘Little Blue Spheroid’ classes). These levels are Spheroid Dominated/Disk Dominated, Single/Multi and Barred/Unbarred, and are discussed here:

Spheroid Dominated/Disk Dominated Galaxies are initially split into spheroid or disk dominated⁷. Colour may be a useful indicator here, however, the apparent gradient and smoothness of the light profile and the central concentration are the main discerning factors.

Single/Multi A question of the total number of distinct structural components comprising the galaxy. Spheroid-dominated single-component galaxies are classical elliptical systems, whereas spheroid-dominated multi-component galaxies are lenticular or early-type spiral systems (S0-Sa). Disk-dominated single-component galaxies are

bulge-less disk systems or irregulars (Sd-Irr), whereas disk-dominated multi-component galaxies are late-type spiral systems (Sab-Scd).

Barred/Unbarred The final level of classification determines whether a multi-component system contains a bar structure. If the disk is edge-on, and the presence of a bar cannot be verified, then the galaxy is classified as unbarred.

At the Spheroid Dominated/Disk Dominated level of classification, two additional classification options are available: stars and ‘Little Blue Spheroids’ (LBS). As noted above, this is the only occasion on which the classification question is not binary.

Stars If the primary object in the postage stamp depicts either a foreground star in front of a background galaxy (for which the associated redshift belongs) or a supernova within a distant galaxy, it is classified as a star. These objects are removed from the classification tree at the top level. This class of object is removed in all subsequent scientific analyses unless specifically mentioned in the text.

Little Blue Spheroids (LBS) Prior to classification it became apparent that an additional type of galaxy which lies outside the standard Hubble-Jeans tuning fork exists within our sample. These galaxies are typically compact, spheroidal and blue, hence their designation as ‘Little Blue Spheroids’ (LBS from here). The median colour of our LBS sample is $g - i \sim 0.6$ with a median Sérsic index of $n_r \sim 1.9$ in the r band ($n_K \sim 1.6$ in the K band) and a median physical size of $r_e \sim 1.1$ kpc in the r band ($r_e \sim 0.9$ kpc in the K band). LBS-type galaxies may come about via the intermittent stochastic star formation predicted in low-mass dwarf galaxies by Stinson et al. (2007), and have been previously isolated observationally by Arp (1965); Sandage & Binggeli (1984); Guzman et al. (1997) and more recently by Brough et al. (2011) and Bauer et al. (2013), amongst others. Brough et al. (2011) finds that these systems are predominantly low-mass and found in low-density environments, showing similar properties to dwarf irregular galaxies in the Local Volume. For the purposes of this study, these objects are removed from the classification tree at the top level.

⁷ Here, the terms ‘spheroid dominated’ and ‘disk dominated’ do not refer to the spheroidal or disk component dominating the total flux of the system. As has been shown in Graham & Worley (2008), rarely does the spheroid component in a bulge+disk system contribute $> 50\%$ of the flux for galaxies later than S0. Rather, we define the term ‘spheroid dominated’ and ‘disk dominated’ to refer to the visual impact of the spheroid or the disk on the postage stamp images; a combination of relative size, apparent surface brightness and 2D light profile.

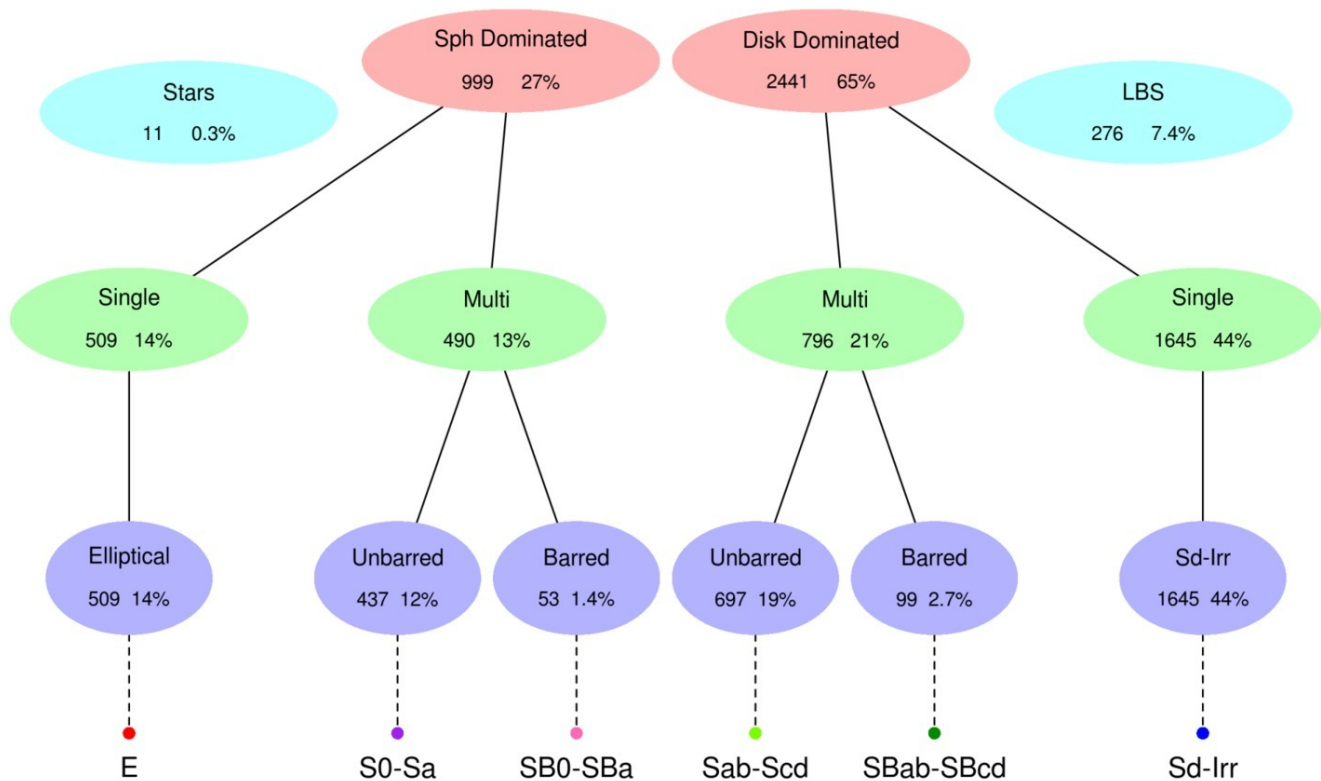


Figure 3. The morphological classification hierarchy used to filter the volume-limited GAMAnear sample of 3,727 galaxies into their appropriate class. In brief: is the galaxy spheroid or disk dominated?; is the galaxy a single component or a multi-component system ('single' and 'multi')?; and, if the galaxy is a multi-component system, does it contain a bar ('unbarred' and 'barred')? At the top level, the classes 'Stars' and little blue spheroids (LBS) are also available. See the text for further details. Beneath each label are the number of galaxies in the master classification bin for that group and an indication of the fraction of our total sample this group constitutes. The final morphological type at the bottom of this figure depends upon the prior decisions made by the classifier.

Three observers; LSK, SPD and ASGR, independently classified the entire sample of 3,727 galaxies using both the phase 1 and phase 2 postage stamp images. Phase 2 postage stamp images are initially placed into their Phase 1 hierarchy positions as assigned by their classifier in order to speed up and improve the second round of classification.

3.2 Classification Results

A final master classification is assigned based on majority agreement. In most cases (i.e., Single/Multi and Barred/Unbarred) this requires the agreement of at least two observers. At the top level (Spheroid Dominated/Disk Dominated, Stars, LBS), there is a possibility that all three observers disagree on the classification. In this instance, a preference is applied to each observer by order of classification experience (in order: SPD, ASGR, LSK). Should a disagreement arise, the classification will default to the preferred observer. These weights also apply at lower levels should a classifier have already been removed from a classification tree at the top level. At the top level, there are 56 such three-way disagreements in our combined GAMAnear sample of 3,727 objects (1.5%). In addition, a total of 451 objects (12.1%) were classified as either 'Star' or 'LBS' by at least one observer. A visual representation of the level of

agreement between classifiers on the three standard questions (Spheroid Dominated/Disk Dominated, Single/Multi, Barred/Unbarred) is shown in Figure 4.

Generally there is good agreement between observers, however; all three observers show a noticeable disagreement on whether a system hosts a bar, which may explain the relatively low bar fraction in our galaxy sample. For our 8 classification bins we find the following 3-way agreement fractions: Spheroid Dominated: 19.2% (714); Disk Dominated: 56.5% (2107); Single: 41.9% (1563); Multi: 23.5% (877); Barred: 2.1% (77); Unbarred: 17.7% (659); Stars: 0.08% (3); LBS: 2.5% (95).

On combining these classification results using the method outlined above, just under half of our sample, 44.1% (1,645), is visually classified as Sd-Irr type, with elliptical galaxies accounting for 13.7% (509) of the sample. Spheroid-dominated multi-component systems account for 13.1% (490) of the sample, of which 10.8% (53) are visually barred. Disk-dominated multi-component systems account for 21.4% (796) of the sample, of which 12.4% (99) are visually barred. Additionally, 0.3% (11) of our sample are classified as 'Stars', and 7.4% (276) as 'Little Blue Spheroids'. These classifications shall be used throughout the remainder of this study.

Example greyscale postage-stamp images for the vari-

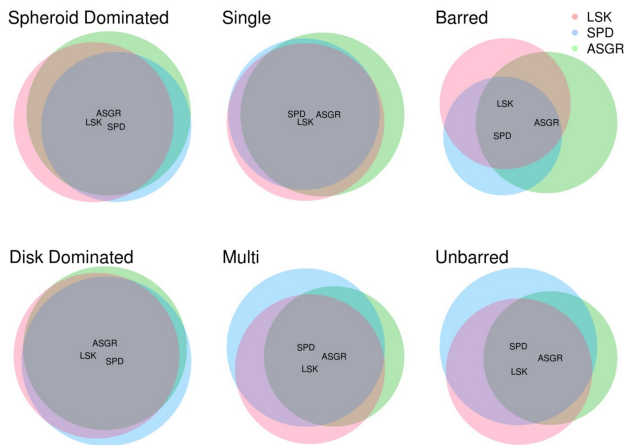


Figure 4. Euler-diagrams representing the level of agreement between the three visual classifiers (LSK, SPD and ASGR) for the six main decision tree classifications; Spheroid Dominated/Disk Dominated, Single/Multi and Barred/Unbarred. Objects where any single classifier classified the system as either ‘Star’ or ‘LBS’ (451 in total) have been removed from this figure, for clarity.

ous visual morphological classes are shown in Figure 5, arranged according to local flow corrected redshift. The Star and LBS classes are included here for reference. A comparison between our own morphological classifications and those of Galaxy Zoo can be found in Appendix B, and further 3-colour postage-stamp examples for each morphological class arranged into a colour-Sérsic index plane may be found in Appendix C.

4 MORPHOLOGICAL TRENDS

4.1 Trends With Global Properties

In Figure 6 we show five global galaxy measurements against one another, coloured according to their morphological classification. The five measurements shown are r band measured half-light radius (kpc), ellipticity as measured in the r band, absolute r band Sérsic magnitude (truncated at $10r_e$), rest-frame $(u - r)$ colour from the best-fitting SED and r band Sérsic index. Sérsic measurements come about from a single-Sérsic fit to the r band data (Kelvin et al. 2012). Absolute Sérsic magnitudes are calculated in the standard sense, using Equation 2.

It can be seen that some projections of the data more easily allow distinct morphological groupings to be brought out than others. Absolute magnitude against half-light radius shows a red-sequence of elliptical-type galaxies progressing from the bright extended end diagonally downwards towards the compact faint region of the figure, slightly exhibiting the curvature that is known to become more apparent at magnitudes fainter than that sampled here (e.g., Binggeli et al. 1984; Graham & Worley 2008; Forbes et al. 2008; Misgeld & Hilker 2011). Note the elliptical galaxy extension of this curved relation in $L-r_e$ space directly into the LBS regime. Clear bimodalities in the data can be seen in the planes of absolute magnitude vs $(u - r)$ colour, absolute magnitude vs Sérsic index, and $(u - r)$ colour vs Sérsic in-

dex. As has been shown in, e.g., Baldry et al. (2004); Driver et al. (2006); Conselice (2006), these bimodal distributions are well fitted by a double-Gaussian profile.

Spheroid-dominated bulge+disk systems (S0-Sa/SB0-SBa) all occupy the same parameter space as the single-component elliptical galaxies, lying on top of the red-sequence. These results are in good agreement with the conclusions of Drory & Fisher (2007), who find that spiral galaxies harbouring classical bulges lie consistently on the red-sequence. However, we do not assert that all S0-Sa galaxies harbour a classical bulge, as has previously been shown for the S0 type galaxy NGC 2787 (Erwin et al. 2003). Although speculation remains as to how $z = 0$ classical bulges came into existence, one hypothesis (Driver et al. 2013) is that they may have formed from the compact elliptical galaxies at $z \sim 2 \pm 0.5$. The evolutionary path of these high-redshift compact galaxies may have diverged from today’s classical bulges, having grown a disk through gas accretion (e.g., Navarro & Benz 1991; Steinmetz & Navarro 2002; Graham 2013) while today’s elliptical galaxies puffed-up via progressive minor accretion events (see Driver et al. 2013, and references therein), but see Carollo et al. (2013). In contrast to classical bulges, pseudo-bulges are believed to form via secular evolutionary processes present within the disk (Debattista et al. 2006; Gadotti 2009; Saha et al. 2012). In brief: if left in isolation for a sufficient length of time (i.e., without any major merging events), a dynamically cold rotating disk system will form a barred structure. In practice, external gravitational triggers (flybys, rather than mergers) are additionally responsible for inducing the formation of bars. The bar acts as a very efficient means by which stellar mass and gas in the disk may be funnelled into the core of the galaxy, initiating a new phase of star formation in the central region. A young, blue sub-structure exhibiting a large component of angular velocity and a flattened 2D-like structure with a low central concentration ($\text{Sérsic } n \lesssim 2$) will form. This new structure is commonly referred to as a pseudo-bulge. We note however that it is possible to form low Sérsic index ($n < 2$) bulges via other non-secular processes (see a full review in Graham 2013). Unlike classical bulges, Drory & Fisher find that galaxies with pseudo-bulges typically lie in the blue cloud (Drory & Fisher 2007). We find very few multi-component systems overlapping with the main body of the blue cloud, and conclude that structural decomposition is required in order to comment further on a) which of these galaxies may contain a pseudo-bulge and b) where these galaxies lie in relation to the blue cloud.

4.2 Trends With Redshift

One would not expect to see large evolutionary variations in morphological fraction over a narrow redshift range such as that used in the creation of our volume limited sample. Figure 7 shows the data as a function of redshift, with data points coloured according to their morphology, as indicated. These data are shown relative to their absolute r band Sérsic magnitudes (top) and number fractions (bottom). Shaded regions indicate $\pm 1\sigma$ binomial confidence intervals (Cameron 2011). One can clearly see the large-scale structure with redshift appearing as over-dense strips in the scatter plot. The two distinctive peaks in the Sd-Irr type galaxy population at redshifts of low density ($z \sim 0.035$ and

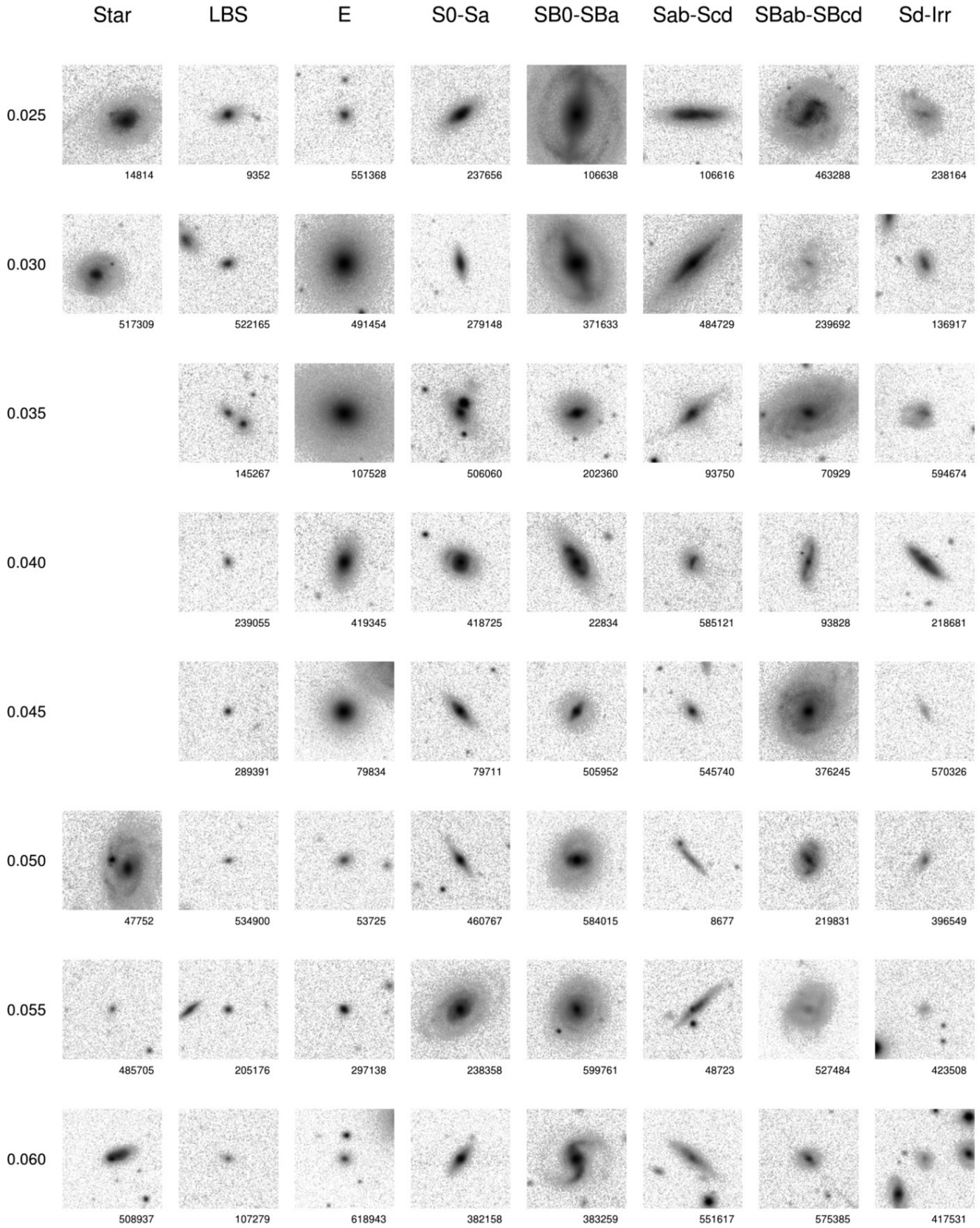


Figure 5. Example postage-stamp cutouts for each morphological class, arranged according to redshift. Below each postage-stamp is the GAMA ID of the galaxy, for reference. The images shown here are created from arctan-scaled composite three-colour images (RGB taken from *Hig*, respectively), with the colours desaturated and inverted to create a greyscale black-on-white image. Blank spaces show regions where no objects of that class exist.

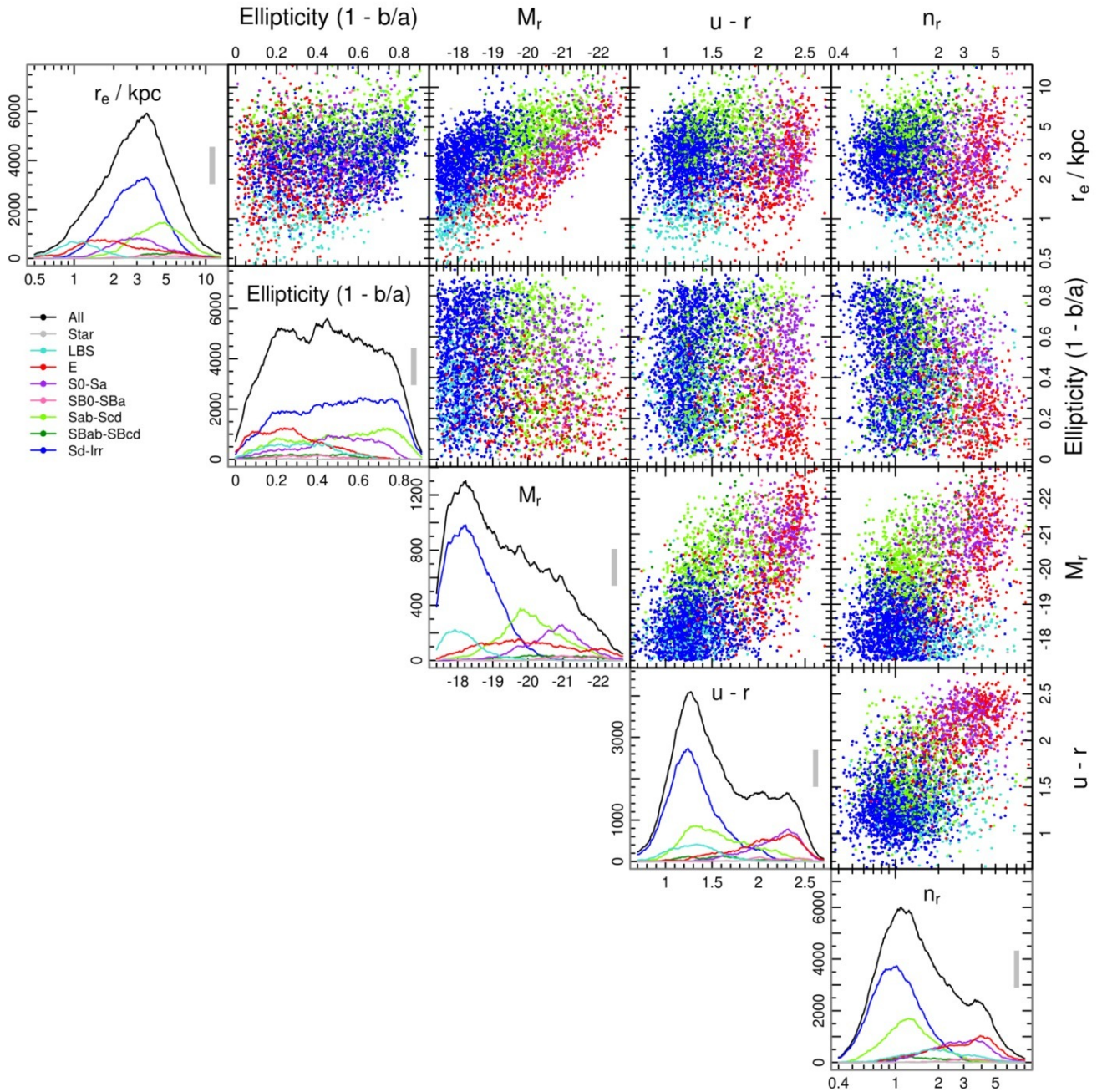


Figure 6. Correlation matrix showing five global parameters, namely (from left to right): r band half-light radius (in kpc), ellipticity, absolute r band Sérsic magnitude, $(u - r)$ rest frame colour from SED fitting and r band Sérsic index. The associated 1D density plots have been constructed using rectangular bandwidth standard deviations of 0.15, 0.09, 0.55, 0.2 and 0.13, respectively, as indicated by the width of the grey rectangles inset into each density sub-plot. The density plots integrate to the total number of objects in each population. Data points are coloured according to their visual morphological classification, as indicated. Distinct groupings of similar colour data points (i.e., same morphology) can be seen, particularly in the case of absolute magnitude against half-light radius where the red-sequence for elliptical galaxies and the blue cloud for Sd-Irr type galaxies is clearly visible.

$z \sim 0.047$) reflect the aforementioned morphology-density relation of Dressler (1980).

Elliptical galaxies (red) exhibit a minor fractional evolution over this redshift range, with a higher proportion of elliptical galaxies at the high redshift end of our sample relative to our lowest redshift bin. Moving from high to low redshift, as the elliptical fraction drops off it is replaced by

Sab-Scd (and, to a lesser extent, SBab-SBcd) type galaxies. However, these trends appear to be minor, and confirm that these data do not show large evolutionary variations in morphological fraction with redshift. Note that we did observe distinct fractional evolutionary trends at redshifts below $z = 0.025$, i.e., our lower limit, however, we give low credence to these results owing to the very low numbers of

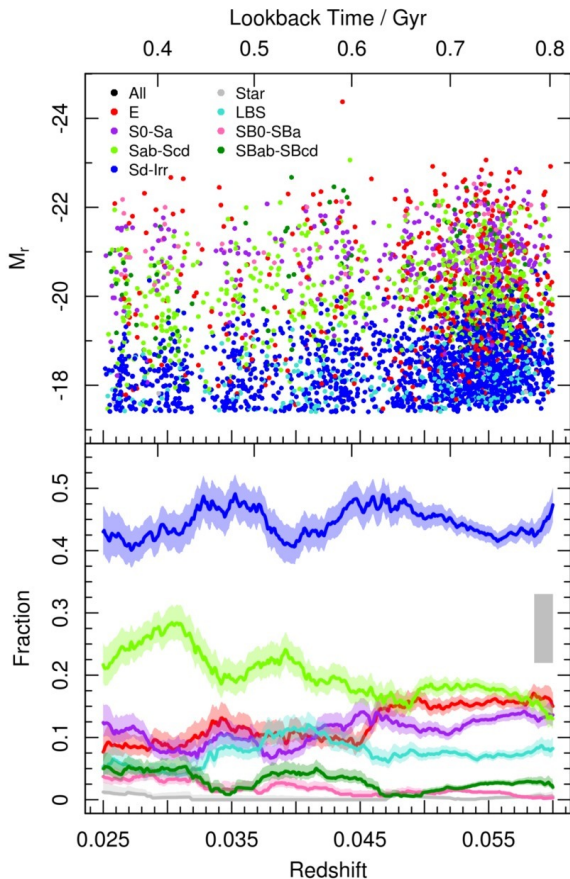


Figure 7. Morphology against redshift. Data points are coloured according to their morphology, as indicated. (top) Absolute r band Sérsic magnitude as a function of redshift. (bottom) The representative fractions of the total number of galaxies for each morphology, as a function of redshift. Shaded regions indicate $\pm 1\sigma$ binomial confidence intervals (Cameron 2011). These fractions have been constructed using a rectangular kernel with a bandwidth standard deviation of 0.005, as indicated by the width of the grey rectangle inset into the lower plot.

galaxies in our volume at $z < 0.025$ (~ 300 galaxies in the redshift range $0.013 < z < 0.025$).

5 LUMINOSITY FUNCTIONS

The luminosity function (LF) describes the number density of galaxies in any given luminosity (or magnitude) bin across a wide range of luminosities. Measurement of the LF allows for constraints to be placed on galaxy formation and evolution models, and as such is valuable and informative.

5.1 The Schechter Luminosity Function

The Schechter (1976) Luminosity Function is an analytical representation of the luminosity function, describing the number of galaxies per unit volume in the luminosity interval L to $L + dL$, where dL is some linear luminosity interval. The number density, $\phi(L) dL = dn$, is given by

$$\phi(L) dL = \phi^* \left(\frac{L}{L^*} \right)^\alpha \exp \left(-\frac{L}{L^*} \right) \frac{1}{L^*} dL \quad (3)$$

where ϕ^* is the normalisation constant, L^* is the characteristic luminosity describing the position of the ‘knee’ in the luminosity function and α gives the slope of the luminosity function at the faint end (where $L \ll L^*$). Note that ϕ^* , L^* and α are to be determined by minimising a fit to the data. The impact of the Schechter function is to truncate the bright-end power law distribution of galaxies, vastly reducing number counts at luminosities brighter than L^* .

It is usually more convenient when considering luminosities to re-write the Schechter Function in terms of magnitude, as given by

$$\Phi(M) dM = 0.4 \ln 10 \cdot \phi^* 10^{-0.4(M-M^*)(\alpha+1)} \times \exp \left(-10^{-0.4(M-M^*)} \right) dM \quad (4)$$

where M and M^* are the magnitude and the characteristic magnitude corresponding to L^* . The parameters α and ϕ^* now correspond to the slope and normalisation constant in magnitude space. Equation 4 is the form of the Schechter function we shall assume throughout the remainder of this paper.

5.2 Measuring the Luminosity Function

The total galaxy luminosity function (GLF) is dominated by large numbers of very faint galaxies, while the space density of brighter galaxies drops off sharply beyond some given luminosity (L^*). Despite their numerical dominance however, low luminosity systems tend to contribute a relatively small fraction to the total luminosity budget of any given volume (Driver 1999). The GLF is a combination of its constituent morphological-type luminosity functions (MLFs), with each morphological type contributing variable number densities, dependent upon magnitude.

Figure 8 shows the GLF and constituent MLFs across nine GAMA wavelengths ($ugrizYJHK$) for our volume-limited GAMAnear sample of 3,727 galaxies. The barred populations have been merged into their sibling classes owing to low number statistics for those two populations. Each population (total and morphological type) is binned into absolute Sérsic magnitude bins of 0.25 mag and fit with a single Schechter function⁸. Errors on each bin are assumed to be Poissonian. Shaded grey areas indicate the limits of the fit beyond which data were not used to constrain the Schechter function model. These limits are a minimum number count of $n \leq 3$ and an absolute Sérsic magnitude faint-end cutoff as given in Table 2.

The knee in the total Schechter function progresses smoothly towards brighter AB magnitudes as one moves from u to K , as expected. We find the knee to be generally well fitted with a single Schechter function until $\sim z$

⁸ Schechter functions are fit to the available data within our magnitude ranges using the NLMINB routine in R; a quasi-Newton algorithm based on the PORT routines that optimise fitting in a similar sense to the Limited-memory Broyden-Fletcher-Goldfarb-Shanno algorithm (LM-BFGS), with an extension to handle simple box constraints on input variables (L-BFGS-B). The PORT documentation is available at <http://netlib.bell-labs.com/cm/cs/cstr/153.pdf>.

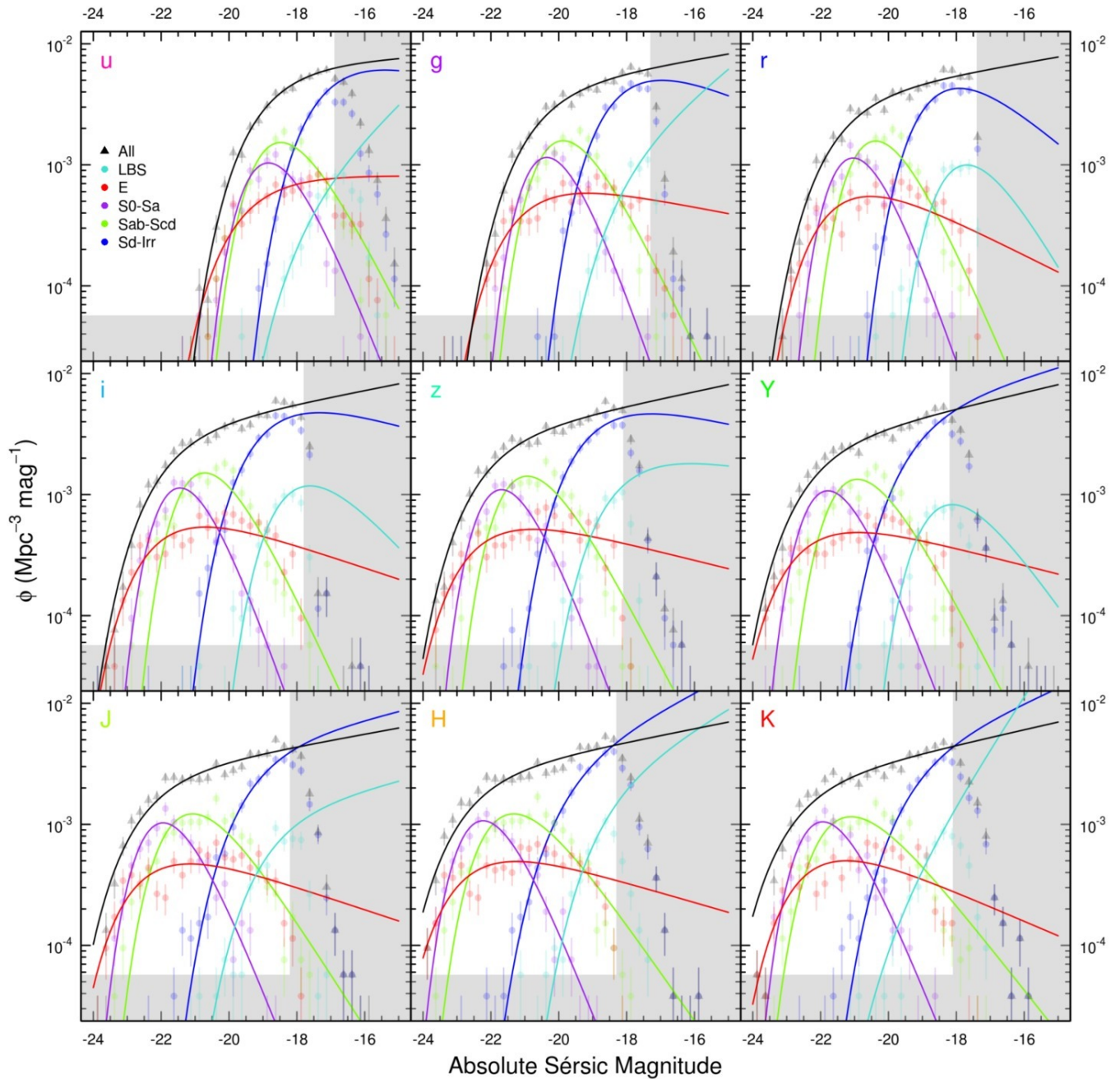


Figure 8. Morphological-type Luminosity Functions across all nine bands for the various morphological types (coloured points and lines, as indicated) and total populations (black points and lines). Each population has been fit with a single Schechter function. Prior to fitting, the data are split into bins of 0.25 mag, with the error on the measurement per bin taken as Poissonian (\sqrt{n}) in nature. Shaded grey areas indicate those regions where data has not been used in the fits. Variable faint-end magnitude limits are given in Table 2.

band. At longer wavelengths, the GLF appears to require a secondary component to aid in fully reproducing the downturn at the bright end and the secondary upturn at the faint end.

These data provide one of the first measurements of the MLF using Sérsic photometry, and provide a key insight into the nature of the underlying galaxy populations. Considering the morphology sub-populations alone, the faint end appears to be heavily dominated by Sd-Irr type galaxies, in addition to a significant LBS fraction. Intermediate mag-

nitudes typically contain both the S0-Sa and Sab-Scd type systems. Elliptical galaxies dominate at the brightest magnitudes, however, below their L^* knee the number of E-type galaxies remains relatively constant across all wavelengths. The Sd-Irr and LBS populations appear to show the largest variation in their MLFs with respect to wavelength, with the faint end slopes varying strongly from u to K as the relative depth of the data in those bands becomes shallower. Owing to our sample selection constraints and the relatively high quality of the r band data, one would expect the M^* and α

parameters for Sd-Irr and LBS type galaxies in the r band to be the most robust in relation to other passbands, which is perhaps evidenced by the suggestion of a downturn in the Sd-Irr type galaxy population at the faintest ($M_r > -18.5$ mag) magnitudes. In contrast, the E, S0-Sa and Sab-Scd populations reproduce consistent luminosity function curves at each wavelength, albeit offset in magnitude.

Single Schechter fit parameters are shown for all populations in Tables 3 (All); 4 (LBS); 5 (E); 6 (S0-Sa); 7 (Sab-Scd) and 8 (Sd-Irr). In addition to the Schechter fit parameters, we also calculate the luminosity density for each population at each wavelength. The luminosity density, j , is the integral under the Schechter function curve and is given by

$$j = \int_0^{\infty} L\phi(L)dL = \phi^* L^* \Gamma(\alpha + 2) \quad (5)$$

as in Liske et al. (2003). Note that the luminosity densities are those calculated from an extrapolation across all luminosities. Also note that the quoted errors on j are likely to be a lower bound owing to the correlation of errors in L^* , α and ϕ^* .

Alongside the characteristic knee in the Schechter luminosity function, L^* (or M^*), the remaining fitted parameters are the slope of the faint end of the LF, α , and the normalisation ϕ^* . While the error on the latter may be estimated via some simplistic method such as jackknife resampling⁹ of the data set, the well-known covariance between α and M^* would result in their jackknife errors being systematically underestimated. An alternative approach is to produce error ellipses which map out the χ^2 parameter space around the best fit values. This technique involves re-fitting the data set fitting for ϕ^* alone while adopting a fixed pair of input α and M^* parameters as defined by a regularly spaced grid about the best fit values. Assuming Gaussian errors, the resultant χ^2 surface then allows for 1, 2 and 3 σ errors to be determined as the contours which lie at $\Delta\chi^2 = 2.30, 6.17$ and 11.8, respectively.

We thus derive error ellipses for all nine photometric bands of our dataset, and show the results in Figure 9. Error ellipses for the total GLF and the constituent MLFs are shown, as indicated. Successive contours represent the 1, 2 and 3 σ errors on each parameter. As can be seen, the strong covariance between these two parameters has a strong impact on each error ellipse. The LBS population shows the largest errors, which should not be surprising considering our sample selection limits and the typically faint magnitude of these systems. The visible truncation of the LBS error ellipses toward the bright end of each figure (with the exception of the r band) is as expected, owing to a lack of LBS type systems at brighter magnitudes. The brightest LBS in our sample has a Sérsic r band magnitude of $M_r = -20.82$ mag. Only the r band data allow any meaningful constraints to be placed on Schechter fit parameters to the LBS population (and to some extent, the Sd population also), particularly in constraining M^* .

Of the standard Hubble types, the faint end slope of

Band	M^* (mag)	α	$\phi^*/10^{-3}$ (mag $^{-1}$ Mpc $^{-3}$)	χ^2/ν	$j/10^7$ (L $_{\odot}$ Mpc $^{-3}$)
u	$-19.18^{+0.13}_{-0.13}$	$-1.05^{+0.09}_{-0.08}$	6.99 ± 1.60	1.12	$12.05^{+0.86}_{-0.86}$
g	$-20.95^{+0.12}_{-0.12}$	$-1.12^{+0.05}_{-0.04}$	4.71 ± 0.37	1.92	$14.00^{+0.51}_{-0.51}$
r	$-21.71^{+0.11}_{-0.11}$	$-1.12^{+0.03}_{-0.03}$	4.00 ± 0.21	2.79	$16.02^{+0.81}_{-0.81}$
i	$-22.15^{+0.10}_{-0.12}$	$-1.14^{+0.04}_{-0.03}$	3.61 ± 0.52	2.46	$19.29^{+1.39}_{-1.39}$
z	$-22.49^{+0.12}_{-0.13}$	$-1.15^{+0.04}_{-0.03}$	3.17 ± 0.22	2.32	$22.89^{+1.30}_{-1.30}$
Y	$-22.61^{+0.13}_{-0.13}$	$-1.16^{+0.03}_{-0.04}$	2.77 ± 0.37	2.25	$22.16^{+1.16}_{-1.16}$
J	$-22.78^{+0.13}_{-0.14}$	$-1.13^{+0.04}_{-0.03}$	2.72 ± 0.27	3.18	$25.90^{+1.64}_{-1.64}$
H	$-23.02^{+0.13}_{-0.13}$	$-1.14^{+0.04}_{-0.03}$	2.73 ± 0.63	4.32	$37.08^{+7.94}_{-7.94}$
K	$-23.06^{+0.19}_{-0.21}$	$-1.16^{+0.04}_{-0.04}$	2.33 ± 0.39	3.11	$52.07^{+5.63}_{-5.63}$

Table 3. Single Schechter luminosity function fit parameters for the total GLF as shown in Figure 8. From left to right, columns are: GAMA passband; the knee in the Schechter function (M^*); the slope of the faint end of the Schechter function (α); the normalisation constant of the Schechter function (ϕ^*); the χ^2 goodness of fit parameter (χ^2/ν), and; the luminosity density (j). Errors on M^* and α are taken from the 1 σ error ellipses shown in Figure 9. All other errors are estimated using the relation $\sigma^2 = \frac{N-1}{N} \sum_{i=1}^N (x_j - x)^2$, where x is the best fit parameter, x_j is the best fit parameter as given from a jackknife resampled variant of the data set and N is the number of jackknife volumes. We adopt $N = 10$.

Band	M^* (mag)	α	$\phi^*/10^{-3}$ (mag $^{-1}$ Mpc $^{-3}$)	χ^2/ν	$j/10^7$ (L $_{\odot}$ Mpc $^{-3}$)
u	$-17.99^{+1.71}_{-4.22}$	$-1.65^{+2.76}_{-1.01}$	0.60 ± 1.98	0.47	$0.85^{+4.60}_{-0.85}$
g	$-18.35^{+1.15}_{-3.70}$	$-1.55^{+1.65}_{-1.07}$	1.29 ± 2.03	0.93	$0.63^{+2.27}_{-0.63}$
r	$-17.45^{+0.49}_{-0.61}$	$0.25^{+1.28}_{-1.05}$	2.87 ± 1.21	1.10	$0.24^{+0.03}_{-0.03}$
i	$-17.88^{+0.69}_{-1.21}$	$-0.21^{+1.87}_{-1.58}$	3.40 ± 2.20	1.32	$0.30^{+0.12}_{-0.12}$
z	$-18.39^{+0.97}_{-3.84}$	$-0.88^{+2.31}_{-1.75}$	2.85 ± 2.97	1.10	$0.40^{+0.93}_{-0.40}$
Y	$-18.11^{+0.75}_{-1.96}$	$0.01^{+1.65}_{-1.87}$	2.45 ± 2.62	1.47	$0.28^{+0.12}_{-0.12}$
J	$-19.06^{+1.07}_{-3.41}$	$-1.17^{+1.47}_{-1.08}$	1.33 ± 2.13	1.72	$0.43^{+1.15}_{-0.43}$
H	$-18.85^{+0.98}_{-3.29}$	$-1.40^{+2.01}_{-1.26}$	2.38 ± 3.90	0.71	$0.94^{+12.61}_{-0.94}$
K	$-20.08^{+1.94}_{-3.14}$	$-2.07^{+1.73}_{-0.59}$	0.22 ± 1.31	0.21	—

Table 4. As Table 3 but for little blue spheroids (LBS).

the Sd-Irr class in the u band, $\alpha_u = -0.82^{+0.61}_{-0.55}$, is particularly poorly constrained owing to the poor quality and relatively shallow depth of the u band in conjunction with the completeness issues for the Sd-Irr population. Conversely, while α is typically well constrained for the elliptical populations, the value of the knee in the Schechter function is not. In the K band for example, the turnover is found at $M_K^* = -22.55^{+0.34}_{-0.38}$ mag; a relatively large uncertainty. Also note the relative consistency between recovered α values for all populations over all wavelengths, excepting the u band and LBS populations as discussed above.

The majority of the morphology sub-populations ap-

⁹ A statistical resampling method designed to estimate sample bias and variance by systematically recomputing our Schechter fit parameters on numerous subsets of our data.

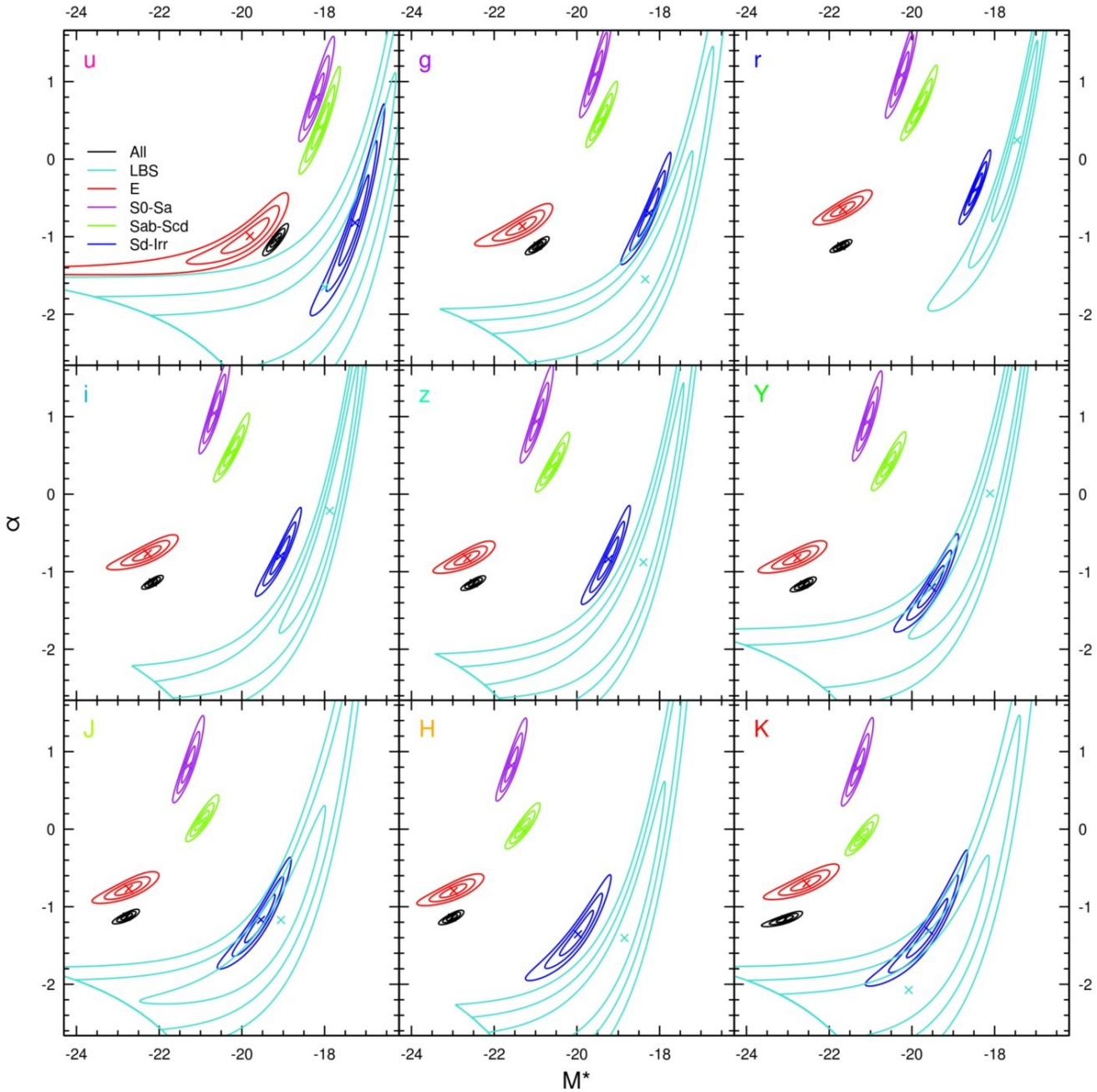


Figure 9. Error ellipses for each Schechter function fit shown in Figure 8. These ellipses are generated by constructing a regularly spaced grid of input M^* and α values in steps of 0.01 each and fitting for the normalisation constant ϕ^* in the Schechter function, producing a χ^2 map about the coordinates of the best fit. Successive contours represent the 1σ , 2σ and 3σ error boundaries ($\Delta\chi^2 = 2.30, 6.17$ and 11.8 respectively). Note the significant diagonal elongation between these parameters, particularly for the Sd class population. This highlights the covariant relationship between M^* and α .

pear to be well fitted by a single Schechter function, with reduced χ^2 values typically lying within the range $0.5 < \chi^2/\nu < 2$. The only notable exceptions to this are for the LBS and the Sab-Scd populations. The knee of the LBS population at most wavelengths lies outside the fitting limits, beyond the faint-end limit, and so the overall fit may instead be better suited by a single exponential function. Note in Table 4 that the slope of the LBS population in the K band is so poorly constrained that the estimated lu-

minosity density diverges, hence no estimate of luminosity density is calculated. The faint-end limit may also affect the Sd-Irr population, particularly in the estimation of the faint end slope, as can be seen in Figure 9. The Sab-Scd population is well described by a single Schechter fit for systems fainter than $M_r \sim -21$ mag, however; at brighter magnitudes the Sab-Scd population departs from a single Schechter form, with number counts at brighter magnitudes very closely matching those of the S0-Sa population. We

Band	M^* (mag)	α	$\phi^*/10^{-3}$ (mag $^{-1}$ Mpc $^{-3}$)	χ^2/ν	$j/10^7$ (L $_{\odot}$ Mpc $^{-3}$)
<i>u</i>	$-19.81^{+0.46}_{-0.69}$	$-0.99^{+0.23}_{-0.22}$	0.92 ± 0.41	0.67	$2.73^{+1.10}_{-1.10}$
<i>g</i>	$-21.32^{+0.33}_{-0.39}$	$-0.86^{+0.11}_{-0.12}$	0.95 ± 0.21	0.96	$3.44^{+0.29}_{-0.29}$
<i>r</i>	$-21.67^{+0.29}_{-0.29}$	$-0.65^{+0.10}_{-0.08}$	1.22 ± 0.19	2.41	$3.88^{+0.37}_{-0.37}$
<i>i</i>	$-22.28^{+0.32}_{-0.36}$	$-0.77^{+0.10}_{-0.09}$	1.04 ± 0.15	1.58	$5.13^{+0.70}_{-0.70}$
<i>z</i>	$-22.65^{+0.29}_{-0.31}$	$-0.83^{+0.09}_{-0.08}$	0.91 ± 0.14	1.60	$6.29^{+0.43}_{-0.43}$
<i>Y</i>	$-22.77^{+0.31}_{-0.35}$	$-0.82^{+0.09}_{-0.08}$	0.86 ± 0.17	1.17	$6.53^{+0.50}_{-0.50}$
<i>J</i>	$-22.73^{+0.30}_{-0.34}$	$-0.77^{+0.09}_{-0.08}$	0.91 ± 0.22	2.27	$6.89^{+0.75}_{-0.75}$
<i>H</i>	$-22.98^{+0.31}_{-0.33}$	$-0.80^{+0.09}_{-0.08}$	0.91 ± 0.15	1.91	$9.91^{+0.98}_{-0.98}$
<i>K</i>	$-22.55^{+0.34}_{-0.38}$	$-0.70^{+0.10}_{-0.09}$	1.05 ± 0.21	3.07	$11.76^{+1.96}_{-1.96}$

Table 5. As Table 3 but for elliptical galaxies.

Band	M^* (mag)	α	$\phi^*/10^{-3}$ (mag $^{-1}$ Mpc $^{-3}$)	χ^2/ν	$j/10^7$ (L $_{\odot}$ Mpc $^{-3}$)
<i>u</i>	$-18.20^{+0.18}_{-0.18}$	$0.80^{+0.31}_{-0.26}$	2.37 ± 0.24	1.53	$2.71^{+0.22}_{-0.22}$
<i>g</i>	$-19.55^{+0.17}_{-0.17}$	$1.09^{+0.31}_{-0.26}$	2.17 ± 0.19	1.45	$3.61^{+0.28}_{-0.28}$
<i>r</i>	$-20.25^{+0.17}_{-0.16}$	$1.08^{+0.30}_{-0.25}$	2.16 ± 0.29	1.60	$4.50^{+0.34}_{-0.34}$
<i>i</i>	$-20.67^{+0.16}_{-0.16}$	$1.04^{+0.29}_{-0.24}$	2.22 ± 0.25	1.18	$5.72^{+0.49}_{-0.49}$
<i>z</i>	$-20.97^{+0.17}_{-0.17}$	$0.94^{+0.28}_{-0.25}$	2.31 ± 0.18	1.23	$6.99^{+0.51}_{-0.51}$
<i>Y</i>	$-21.08^{+0.15}_{-0.15}$	$0.93^{+0.26}_{-0.23}$	2.27 ± 0.32	0.71	$7.39^{+0.62}_{-0.62}$
<i>J</i>	$-21.30^{+0.16}_{-0.16}$	$0.82^{+0.25}_{-0.22}$	2.33 ± 0.37	1.25	$8.82^{+0.80}_{-0.80}$
<i>H</i>	$-21.58^{+0.15}_{-0.16}$	$0.82^{+0.24}_{-0.21}$	2.43 ± 0.32	0.87	$13.63^{+1.36}_{-1.36}$
<i>K</i>	$-21.31^{+0.16}_{-0.17}$	$0.78^{+0.26}_{-0.22}$	2.43 ± 0.17	1.03	$16.02^{+1.19}_{-1.19}$

Table 6. As Table 3 but for S(B)0-S(B)a galaxies.

Band	M^* (mag)	α	$\phi^*/10^{-3}$ (mag $^{-1}$ Mpc $^{-3}$)	χ^2/ν	$j/10^7$ (L $_{\odot}$ Mpc $^{-3}$)
<i>u</i>	$-18.10^{+0.21}_{-0.22}$	$0.41^{+0.31}_{-0.28}$	4.20 ± 0.27	2.03	$3.27^{+0.28}_{-0.28}$
<i>g</i>	$-19.43^{+0.17}_{-0.15}$	$0.51^{+0.19}_{-0.17}$	4.19 ± 0.16	3.20	$3.80^{+0.37}_{-0.37}$
<i>r</i>	$-19.83^{+0.19}_{-0.19}$	$0.65^{+0.22}_{-0.19}$	3.90 ± 0.30	4.54	$3.81^{+0.47}_{-0.47}$
<i>i</i>	$-20.25^{+0.18}_{-0.19}$	$0.54^{+0.20}_{-0.18}$	3.95 ± 0.16	4.33	$4.55^{+0.48}_{-0.48}$
<i>z</i>	$-20.60^{+0.18}_{-0.17}$	$0.36^{+0.17}_{-0.15}$	3.96 ± 0.10	3.79	$5.44^{+0.54}_{-0.54}$
<i>Y</i>	$-20.57^{+0.18}_{-0.18}$	$0.37^{+0.17}_{-0.15}$	3.72 ± 0.13	4.73	$4.95^{+0.49}_{-0.49}$
<i>J</i>	$-20.97^{+0.17}_{-0.17}$	$0.10^{+0.14}_{-0.11}$	3.59 ± 0.41	3.46	$6.19^{+0.74}_{-0.74}$
<i>H</i>	$-21.32^{+0.18}_{-0.18}$	$0.01^{+0.13}_{-0.12}$	3.61 ± 0.23	3.57	$9.38^{+1.02}_{-1.02}$
<i>K</i>	$-21.23^{+0.17}_{-0.16}$	$-0.11^{+0.12}_{-0.10}$	3.40 ± 0.29	3.35	$12.03^{+1.04}_{-1.04}$

Table 7. As Table 3 but for S(B)ab-S(B)cd galaxies.

Band	M^* (mag)	α	$\phi^*/10^{-3}$ (mag $^{-1}$ Mpc $^{-3}$)	χ^2/ν	$j/10^7$ (L $_{\odot}$ Mpc $^{-3}$)
<i>u</i>	$-17.26^{+0.33}_{-0.39}$	$-0.82^{+0.61}_{-0.55}$	10.74 ± 2.81	0.42	$2.84^{+0.74}_{-0.74}$
<i>g</i>	$-18.25^{+0.23}_{-0.27}$	$-0.70^{+0.32}_{-0.29}$	10.55 ± 1.17	1.72	$2.17^{+0.12}_{-0.12}$
<i>r</i>	$-18.46^{+0.16}_{-0.16}$	$-0.40^{+0.22}_{-0.19}$	11.56 ± 0.50	1.08	$1.91^{+0.06}_{-0.06}$
<i>i</i>	$-19.07^{+0.23}_{-0.24}$	$-0.80^{+0.26}_{-0.23}$	8.73 ± 1.33	2.09	$2.27^{+0.13}_{-0.13}$
<i>z</i>	$-19.24^{+0.24}_{-0.26}$	$-0.84^{+0.29}_{-0.26}$	7.97 ± 1.38	1.55	$2.40^{+0.15}_{-0.15}$
<i>Y</i>	$-19.52^{+0.29}_{-0.34}$	$-1.20^{+0.27}_{-0.26}$	5.26 ± 1.86	0.73	$2.54^{+0.30}_{-0.30}$
<i>J</i>	$-19.54^{+0.34}_{-0.39}$	$-1.17^{+0.32}_{-0.29}$	4.65 ± 0.98	1.66	$2.31^{+0.13}_{-0.13}$
<i>H</i>	$-19.97^{+0.36}_{-0.44}$	$-1.36^{+0.31}_{-0.27}$	3.66 ± 1.50	1.47	$3.82^{+0.60}_{-0.60}$
<i>K</i>	$-19.59^{+0.45}_{-0.54}$	$-1.31^{+0.41}_{-0.34}$	3.97 ± 1.70	2.52	$4.25^{+0.82}_{-0.82}$

Table 8. As Table 3 but for Sd-Irr galaxies.

find that a double Schechter fit to this Sab-Scd population is similarly recalcitrant, and so we elect to maintain a single Schechter fit to the Sab-Scd population.

It is evident however that at wavelengths longer than the *z* band a single Schechter fit to the total GLF is a poor fit, reaching a peak goodness of fit value of $\chi^2/\nu = 4.31$ in the *H* band. This is as expected if one considers that the field galaxy LF is comprised of an initial red spheroidal ‘bump’ at bright magnitudes and then a subsequent blue disk ‘bump’ at fainter magnitudes, as can clearly be seen in Figure 8, and noted in, e.g., Phillipps & Driver (1995); Popesso et al. (2006); Loveday et al. (2012). A single Schechter function is unable to account for the intricacy in this distribution.

We elect to fit the total GLF with a double Schechter function with a shared knee, while maintaining single Schechter fits to the morphology sub-populations. The free parameters for the double Schechter fit are M^* , α_1 , ϕ_1^* , α_2 and ϕ_2^* . The results of this fit are shown in Figure 10 for all nine bands, and the fit parameters given in Table 9. It is instantly apparent once more that the GLF is more naturally fit with a double Schechter function than a single Schechter function, particularly so for the longer NIR wavelengths. All χ^2 values beyond the *z* band show a significant improvement in the quality of the fit. However, the shortest wavelengths show little need for the extra parameters, with the goodness of fit showing a mild worsening in the *u* band, again most likely owing to the poorer quality of the *u* band data. Nevertheless, the overall fits appear robust, and so we advocate a double Schechter form for the field total GLF but single Schechter function forms for the morphology sub-population MLFs.

A summary of both the single and double Schechter fits to the GLF in addition to the adopted single Schechter fits to the MLFs in the *r* band are shown in Figure 11. Also shown are several other contemporary single Schechter fits to similar *r* band data, scaled to our preferred cosmology of $(H_0, \Omega_m, \Omega_\Lambda) = (70, 0.3, 0.7)$ and *k*-corrected where necessary from $r^{0.1}$ back to a $z = 0$ rest frame using a typical correction of $k_{0.1} = 0.12$. There is generally good agreement between our global luminosity function fits and those of other studies. The variable faint end limit between surveys makes a comparison of the faint end slope problematic,

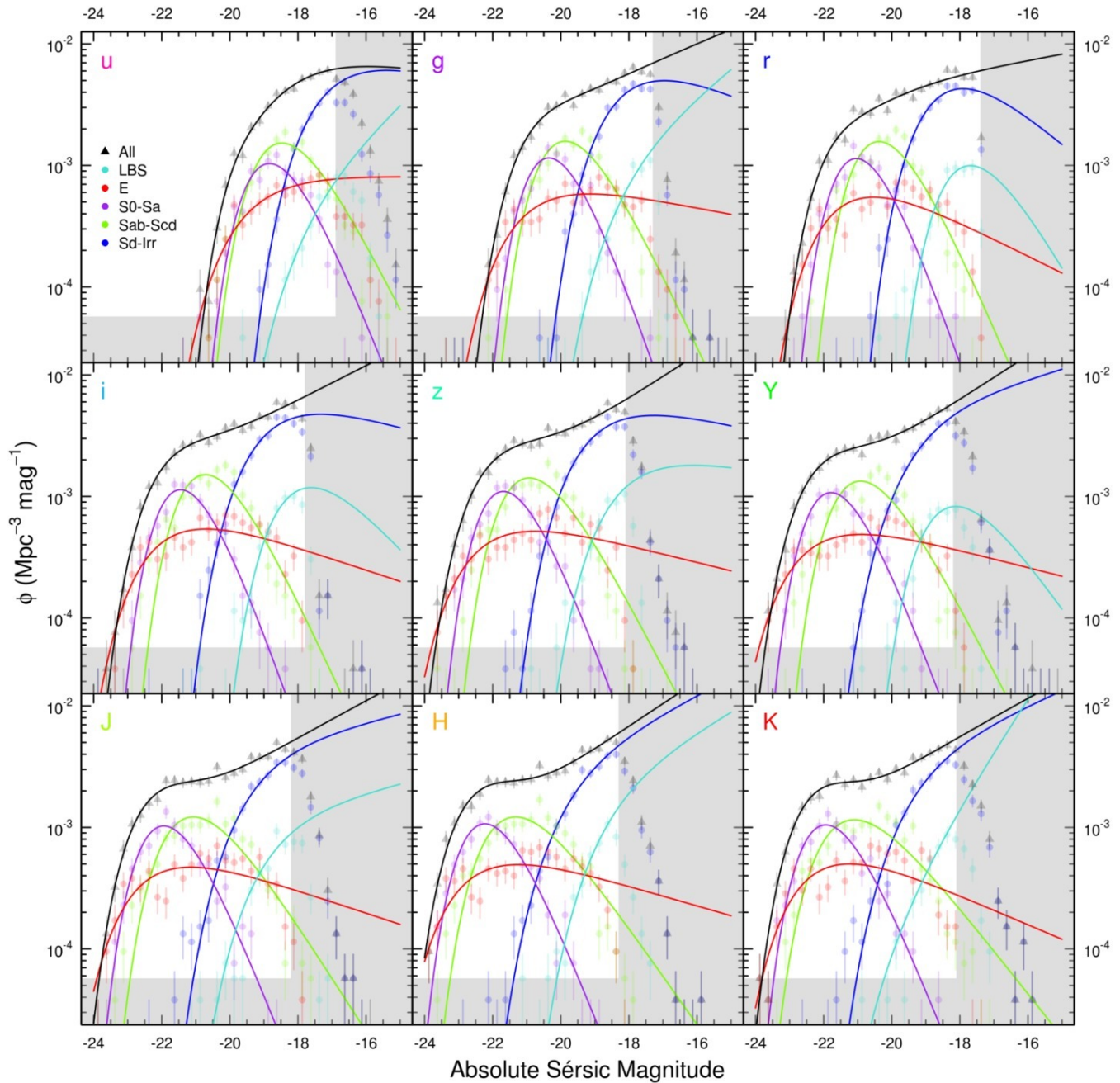


Figure 10. Morphological-type luminosity functions across all nine bands for the various morphological types (coloured points and lines, as indicated) and total populations (black points and lines). Each morphological population has been fit with a single Schechter function and is identical to those shown in Figure 8. Total populations have been fit with a double Schechter function. Prior to fitting, the data are split into bins of 0.25 mag, with the error on the measurement per bin taken as Poissonian (\sqrt{n}) in nature. Shaded grey areas indicate those regions where data has not been used in the fits. Variable faint-end magnitude limits are given in Table 2. The additional Schechter function for the total population allows for the notable upturn at faint magnitudes to be properly accounted for, especially at longer wavelengths.

however, the M^* and ϕ^* parameters agree well to within their errors. The need for a second Schechter component in the r band is less evident than at longer wavelengths, however, its effects in causing a steeper drop off at the bright end can clearly be seen in improving the fit to the data.

6 THE COSMIC SPECTRAL ENERGY DISTRIBUTION BY HUBBLE TYPE

The morphological classifications derived in Section 3 are useful for many purposes beyond measuring the luminosity distributions listed in Tables 3 to 9. One in particular is the subdivision of the cosmic spectral energy distribu-

Band	M^* (mag)	α_1	$\phi_1^*/10^{-3}$ (mag $^{-1}$ Mpc $^{-3}$)	α_2	$\phi_2^*/10^{-3}$ (mag $^{-1}$ Mpc $^{-3}$)	χ^2/ν	$j/10^7$ (L $_{\odot}$ Mpc $^{-3}$)
<i>u</i>	-18.53 ± 1.25	-0.91 ± 7.17	9.64 ± 12.91	1.25 ± 6.01	1.46 ± 9.39	1.23	$11.88^{+2.04}_{-2.04}$
<i>g</i>	-20.28 ± 0.26	-1.29 ± 0.14	3.51 ± 1.75	0.06 ± 0.59	4.88 ± 1.22	1.43	$14.16^{+0.58}_{-0.58}$
<i>r</i>	-20.90 ± 0.26	-1.13 ± 0.07	4.51 ± 1.03	0.53 ± 0.56	3.01 ± 0.83	2.71	$15.84^{+0.71}_{-0.71}$
<i>i</i>	-21.45 ± 0.20	-1.35 ± 0.21	2.20 ± 1.50	-0.09 ± 0.48	4.87 ± 1.34	1.41	$19.75^{+0.85}_{-0.85}$
<i>z</i>	-21.78 ± 0.25	-1.46 ± 0.21	1.40 ± 1.12	-0.26 ± 0.44	5.05 ± 0.88	1.25	$23.31^{+1.36}_{-1.36}$
<i>Y</i>	-21.76 ± 0.24	-1.45 ± 0.23	1.44 ± 1.25	-0.10 ± 0.54	4.83 ± 0.84	0.68	$22.67^{+1.09}_{-1.09}$
<i>J</i>	-21.82 ± 0.17	-1.38 ± 0.13	1.58 ± 0.76	0.08 ± 0.35	4.78 ± 0.72	1.27	$26.00^{+1.36}_{-1.36}$
<i>H</i>	-22.04 ± 0.26	-1.46 ± 2.43	1.35 ± 6.33	0.08 ± 2.58	5.30 ± 6.69	1.21	$38.78^{+3.01}_{-3.01}$
<i>K</i>	-21.72 ± 0.23	-1.39 ± 1.62	1.64 ± 3.13	0.24 ± 1.55	5.09 ± 3.18	0.86	$47.13^{+3.10}_{-3.10}$

Table 9. Double Schechter luminosity function fit parameters for the total GLF as shown in Figure 10. From left to right, columns are: GAMA passband; the shared knee in the Schechter function (M^*); the primary slope of the faint end of the Schechter function (α_1); the primary normalisation constant of the Schechter function (ϕ_1^*); the secondary slope of the faint end of the Schechter function (α_2); the secondary normalisation constant of the Schechter function (ϕ_2^*); the χ^2 goodness of fit parameter (χ^2/ν), and; the luminosity density (j). Errors are estimated from jackknifed resampling using the relation $\sigma^2 = \frac{N-1}{N} \sum_{i=1}^N (x_j - x)^2$, where x is the best fit parameter, x_j is the best fit parameter as given from a jackknife resampled variant of the data set and N is the number of jackknife volumes. We adopt $N = 10$.

tion (CSED; Hill et al. 2010)¹⁰ by morphological type. The CSED can be derived from the fitted luminosity functions, or directly by summing the flux from a volume-limited galaxy sample observed across a broad wavelength range (see Driver et al. 2012 for a discussion of the two methods, with the latter generally being favoured if the data are sufficiently deep). The CSED describes the instantaneous attenuated energy production rate of the Universe today. The energy budget, like the mass budget, is a fundamental description of the Universe which can be readily compared to complex (e.g., Somerville et al. 2012) or basic (e.g., Driver et al. 2013) model prescriptions.

At the present epoch the energy production budget is almost entirely dominated and driven by stellar nucleosynthesis combined with dust re-processing of the emergent starlight (i.e., the AGN contribution at very low redshift is negligible, see Driver et al. 2012). Because of this latter effect the CSED comes in two flavours, attenuated (i.e., as observed) and unattenuated (i.e., dust corrected), both of which are useful. For example to measure the global star-formation rate of a specific sub-population one desires the unattenuated CSED, but to quantify the ambient intergalactic UV flux one requires the attenuated CSED.

While the attenuated CSED is straight-forward to derive, the unattenuated CSED requires a correction for the wavelength and inclination dependent photon escape fraction. The *FUV* to *K* photon-escape fraction, integrated over all inclinations for the zero redshift galaxy population, was recently quantified by Driver et al. (2007, 2008) using data

from the Millennium Galaxy Catalogue (MGC; Liske et al. 2003; Driver et al. 2005). Here the MGC data was used to constrain the face-on central opacity ($\tau_B \sim 3.8$) of the disk galaxy population (Driver et al. 2007) by comparison of the inclination dependent B_{MGC} -band M^* value, with predictions from the detailed radiative transfer modelling described in Popescu et al. 2011 (see also Popescu et al. 2000 and Tuffs et al. 2004). It is worth noting that this dust prescription incorporates full radiative transfer treatment including anisotropic scattering processes from within three distinct dust components: an extended optically thin double exponential dust disc, a compact optically thick double exponential dust disc, and clumpy components associated with star forming complexes, with a prescription that allows for cloud fragmentation (Tuffs et al. 2004).

Here we report the contribution of each morphological type to both the attenuated and unattenuated CSED using the photon escape fraction described above for the S(B)ab-S(B)cd, Sd-Irr, and LBS populations, and assuming the E and S(B)0-S(B)a populations are dust free. We opt to dust correct LBS galaxies after a non-exhaustive examination of the spectra of a large number of these systems wherein we found repeated evidence for ongoing star formation. While Sa galaxies in our sample may indeed contain dust, we assume that to first order a correction of this type is broadly correct. Note that Rowlands et al. (2012) recently showed from Herschel-ATLAS data that at most 10% of the elliptical population contains dust (see also Agius et al. 2013). In due course the variation of dust properties with morphological type will be investigated using the *FUV* to far-IR GAMA multi-wavelength dataset (see Driver et al., in prep).

6.1 Measuring the integrated fluxes

Any description of the CSED will be incomplete without the inclusion of *FUV* and *NUV* estimates. This is because

¹⁰ The CSED is distinct to the energy in photons within a fixed volume (see for example Domínguez et al. 2011), as the majority of these were generated at earlier epochs (i.e., the CSED is the instantaneous energy production rate whereas the extragalactic background light is the integrated energy production incorporating cosmological effects).

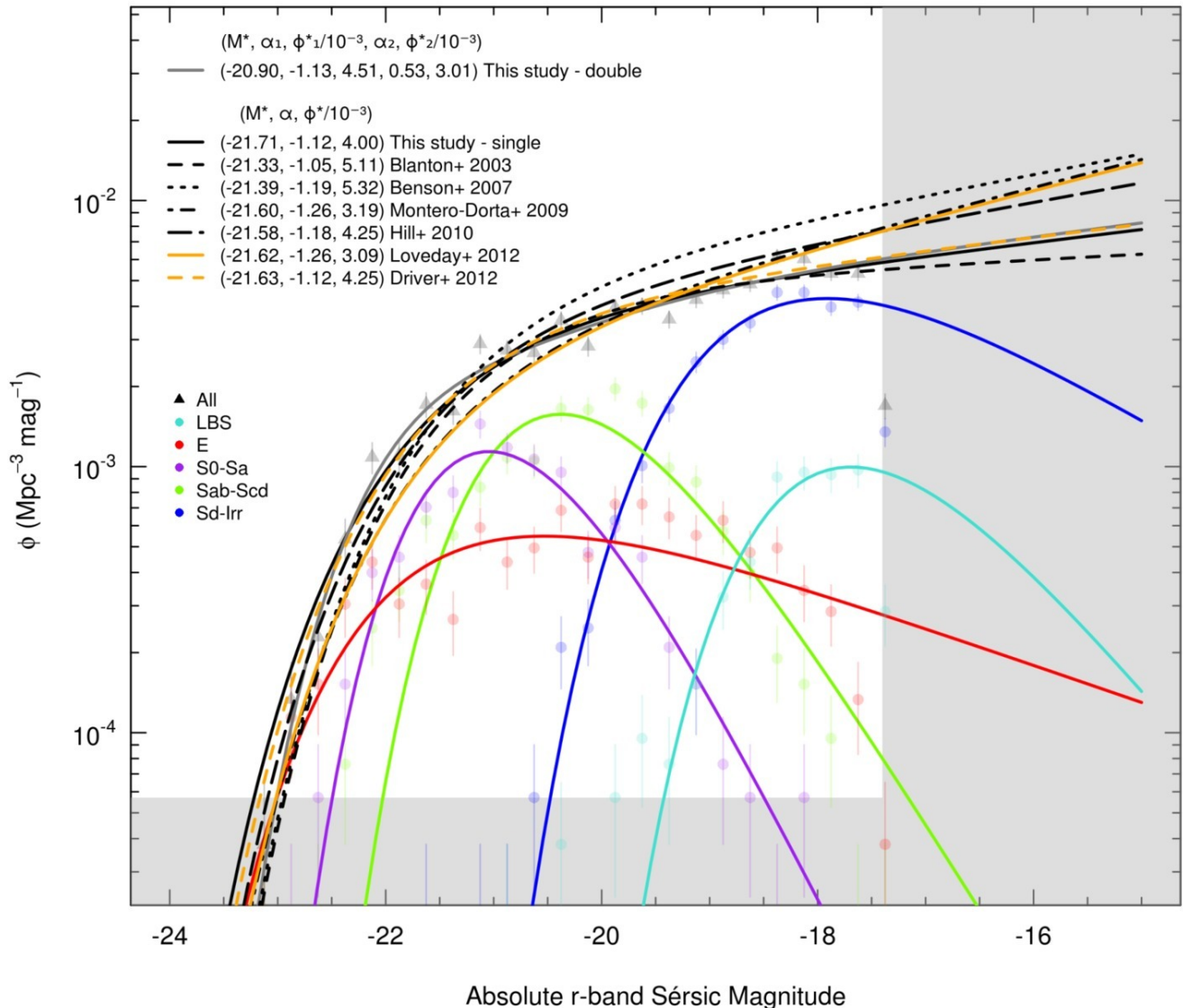


Figure 11. Morphological-type luminosity functions in the r band fit by single-Schechter functions in addition to the total luminosity function fit by both a single and double-Schechter function, shown in grey and black respectively. Each morphology is labelled and coloured according to the inset legend. Prior to fitting, the data are split into bins of 0.25 mag, with the error per bin assumed as Poissonian (\sqrt{n}) in nature. Shaded grey areas ($M > -17.4$ mag and $n \leq 3$) indicate those regions where data has not been used in constraining the Schechter fits. Schechter fit parameters from the global fits (inset, top left) in addition to single-Schechter fits from other studies are also shown, for reference. Where appropriate, Schechter fit data from other studies has been k -corrected from $z = 0.1$ back to a $z = 0$ rest frame using a typical correction of $k_{0.1} = 0.12$. Blanton et al. 2003; Montero-Dorta & Prada 2009; Loveday et al. 2012 have been corrected in this fashion, whereas Benson et al. (2007); Hill et al. (2010); Driver et al. (2012) have not. Note that the Benson et al. (2007) values have been scaled up by a factor of 10.

almost 40% of the energy of a global population emerges at wavelengths below 400nm (Driver et al. 2012). Rather than computing the full Sérsic luminosity functions as we have done in the *ugrizYJHK* bands, here we simply elect to sum the FUV and NUV flux for the distinct samples directly and divide by the volume probed. Our FUV and NUV data are taken from the GALEX satellite, specifically; a combination of Medium Imaging Survey (MIS) archival and proprietary data obtained by the MIS and GAMA teams (see Driver et al. 2012 for further details).

Table 10 shows the luminosity density values derived

directly by summing the fluxes of all systems within our volume and for each population. Only galaxies which lie in the common region (i.e., sampled by all 11 bands, see Driver et al. 2012) are included and the volume is modified accordingly to compensate ($\times 0.86$). The luminosity densities shown in Table 10 can be compared to those derived from the fitted Schechter functions in Tables 3 to 9. As discussed in Driver et al. (2012), discrepancies between these two estimates can arise from the extrapolation of the fitted Schechter function combined with sub-optimal fits around the L^* -region. The sum of these values for the individual

Hubble Type	<i>SFR</i> ($M_{\odot} \text{ yr}^{-1} \text{ Mpc}^{-3}$)	<i>SFR</i> Contribution %
All	0.0125 ± 0.0030	100
E	0.0001 ± 0.0001	1
S(B)0-S(B)a	0.0020 ± 0.0003	16
S(B)ab-S(B)cd	0.0073 ± 0.0011	58
Sd-Irr	0.0031 ± 0.0005	25
LBS	$< 0.0001 \pm 0.0001$	< 1

Table 11. The star-formation rate density for each morphological type as derived from the FUV luminosity densities reported in Table 10.

morphological classes also agree well with the global values reported in Driver et al. (2012), implying internal consistency between the various GAMA sub-samples and methodologies. In detail the FUV and NUV values reported here are lower which is also consistent with the slightly lower median redshift given the steeply declining cosmic star-formation history (see for example Hopkins & Beacom 2006; Driver et al. 2013) — i.e., $z \sim 0.04$ versus $z \sim 0.08$, equivalent to a time interval of ~ 0.5 Gyr. Note, from Driver et al. (2013), we expect the mean cosmic star formation rate at $z = 0.06$ to be $\sim 22\%$ higher than at $z = 0$.

6.2 Star-formation rates by morphological type

The dust corrected FUV luminosity density can be converted directly to a measure of the star-formation rate. These values are shown in Table 11 and assume a photon escape fraction of 23%. In brief, this photon escape fraction is determined by deriving the galaxy luminosity function in the *B* band for galaxies taken from the Millennium Galaxy Catalogue (Liske et al. 2003), subdivided by inclination. The trends in M^* with $\cos(i)$ are compared to those predicted by the complex dust models of Tuffs et al. (2004) (see also Popescu et al. 2011), and used to constrain the face on central opacity (Driver et al. 2007). In Driver et al. (2008), this value is used to predict the average photon escape fraction as a function of wavelength (see Table 3 of Driver et al. 2012). We use the standard prescription by Kennicutt (1989) to derive the star-formation rate which is based on a Salpeter (1955) initial mass-function. The values reported in Table 11 are typically $\times 2$ higher than those reported by James et al. (2008, see their Figure 7). As no evolutionary corrections to the magnitudes are applied, these values correspond to a measurement of the star-formation rate at the median redshift of $z \sim 0.04$ (again, a ~ 0.5 Gyr time interval). Additionally, our ‘All’ measurement is approximately two times lower than that reported in Robotham & Driver (2011), which is again consistent when taking into account the median redshift offset between these two datasets. Our data also confirm the trend seen by James et al. (2008), that the SFR density in the nearby Universe is dominated by the intermediate S(B)ab-S(B)cd Hubble types, with a sharp decline towards earlier or later types.

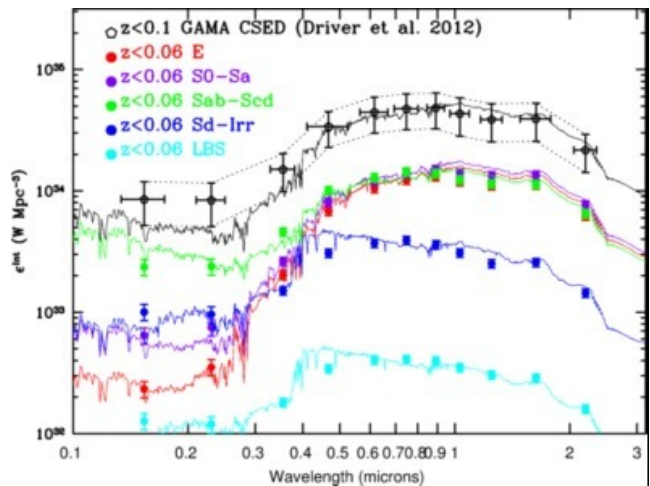


Figure 12. The attenuated (as observed) CSED. Integration under each line provides a direct measure of the emergent observed instantaneous energy production for each galaxy population.

6.3 The attenuated CSED

Figure 12 shows the full *FUV* to *K* attenuated CSED (i.e., as observed) for each of the populations. Overlaid as black data points is the global CSED reported in Driver et al. (2012) derived for the full GAMA $z < 0.1$ sample. Note the earlier data include the sample variance uncertainty indicated by the error bars and dotted uncertainty ranges. As here we are interested in the variations between the morphological types within a single volume we do not include the cosmic variance errors. For each morphological type we fit a range of single stellar population (SSP) PEGASE models (see Fioc & Rocca-Volmerange 1999) to our data. The best fits are shown in Figure 12 by the colour indicated in the key. The sum of these fits is shown as the black curve which agrees well with the $z < 0.1$ CSED showing only a slight discrepancy in the UV where one might expect a slightly reduced CSED due to the declining star-formation rate from $z = 0.08$ to $z = 0.04$ (i.e., $\Delta t \sim 0.5$ Gyr). We do not report the PEGASE values for these curves as they are simply being used here as appropriate fitting functions. Integrating these functions therefore provides a direct measure of the instantaneous energy production emerging from each galaxy population. The total energy output is $(8.53 \pm 0.20) \times 10^{34} \text{ W Mpc}^{-3}$ with approximate subdivisions of 27 per cent, 31 per cent, 32 per cent, 9 per cent, and 1 per cent arising from the E, S(B)0-S(B)a, S(B)ab-S(B)cd, Sd-Irr and LBS populations respectively. This is surprisingly well balanced and shows that all galaxy types contribute significantly to the ambient inter-galactic radiation field, i.e., ~ 58 per cent spheroid-dominated and ~ 42 per cent disk-dominated.

6.4 The unattenuated CSED

Figure 13 shows the unattenuated (corrected) CSED for each of the populations by applying the photon escape fraction prescription determined in Driver et al. (2008) to the S(B)ab-S(B)cd, Sd-Irr, and LBS populations only. Similarly these data are fitted to a range of PEGASE SSP model as before and integrated to give the instantaneous energy production of $(1.12 \pm 0.15) \times 10^{35} \text{ W Mpc}^{-3}$ approximately

Wavelength		Hubble type					
band	(μm)	All	E	S(B)0-S(B)a	S(B)ab-S(B)cd	Sd-Irr	LBS
$10^7 \text{L}_{\odot} \text{Mpc}^{-3}$							
FUV	0.153	16378.14 \pm 2504.93	699.05 \pm 106.91	1928.87 \pm 295.01	7069.65 \pm 1081.25	3010.56 \pm 460.44	380.42 \pm 58.18
NUV	0.230	115.64 \pm 17.69	7.30 \pm 1.12	15.56 \pm 2.38	49.45 \pm 7.56	19.95 \pm 3.05	2.48 \pm 0.38
u	0.355	11.93 \pm 0.95	1.95 \pm 0.16	2.53 \pm 0.20	4.44 \pm 0.36	1.45 \pm 0.12	0.17 \pm 0.01
g	0.467	12.56 \pm 1.01	2.78 \pm 0.22	3.30 \pm 0.26	4.11 \pm 0.33	1.25 \pm 0.10	0.14 \pm 0.01
r	0.616	15.13 \pm 1.21	3.77 \pm 0.30	4.32 \pm 0.35	4.64 \pm 0.37	1.33 \pm 0.11	0.15 \pm 0.01
i	0.747	18.05 \pm 1.44	4.68 \pm 0.37	5.32 \pm 0.43	5.45 \pm 0.44	1.49 \pm 0.12	0.16 \pm 0.01
z	0.892	21.54 \pm 1.72	5.83 \pm 0.47	6.66 \pm 0.53	6.22 \pm 0.50	1.61 \pm 0.13	0.18 \pm 0.01
Y	1.030	22.06 \pm 1.76	6.05 \pm 0.48	7.08 \pm 0.57	6.24 \pm 0.50	1.56 \pm 0.12	0.18 \pm 0.01
J	1.248	25.80 \pm 2.06	7.10 \pm 0.57	8.56 \pm 0.68	7.32 \pm 0.59	1.61 \pm 0.13	0.20 \pm 0.02
H	1.631	38.41 \pm 3.07	10.65 \pm 0.85	12.88 \pm 1.03	10.80 \pm 0.86	2.46 \pm 0.20	0.27 \pm 0.02
K	2.201	45.60 \pm 3.65	12.47 \pm 1.00	15.40 \pm 1.23	12.95 \pm 1.04	2.88 \pm 0.23	0.32 \pm 0.03

Table 10. Luminosity densities as a function of wavelength and morphological type.

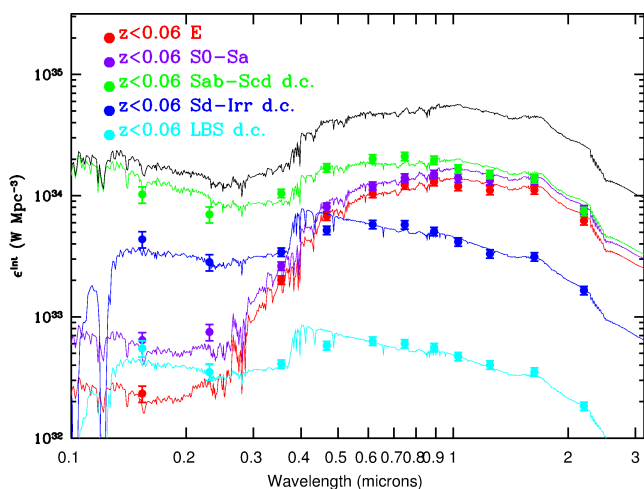


Figure 13. The unattenuated (corrected) CSED. Integration under each line provides a direct measure of the emergent corrected instantaneous energy production for each galaxy population.

subdivided by 21 per cent, 23 per cent, 44 per cent, 11 per cent and 1 per cent for the E, S(B)0-S(B)a, S(B)ab-S(B)cd, Sd-Irr and LBS populations respectively. Hence we see that although the energy which enters into the IGM is dominated 58:42 by spheroid-dominated:disk-dominated types the actual energy production rate is almost inverted, i.e., 44:56 spheroid-dominated:disk-dominated.

7 CONCLUSIONS

We have defined a local ($0.025 < z < 0.06$) volume limited sample of 3,727 galaxies (GAMAnear) taken from the Galaxy And Mass Assembly survey (GAMA; Driver et al. 2009). Using GAMA-reprocessed 9 band imaging from the SDSS (*ugriz*; York et al. 2000; Abazajian et al. 2009) and UKIDSS-LAS (*YJHK*; Lawrence et al. 2007) surveys, we

provide robust visual classifications for each galaxy in our sample into its morphological Hubble type (E, S(B)0-S(B)a, S(B)ab-S(B)cd, Sd-Irr), alongside an additional ‘little blue spheroid’ (LBS) class; a class of potential blue dwarf ellipticals, and a contaminant ‘Star’ class. Approximately 27% of this sample is visually classified as spheroid dominated, with the remaining $\sim 73\%$ visually classified as disk dominated or LBS. We explore morphological trends with several global measurements, namely; *r* band half-light radius (kpc); ellipticity as measured in the *r* band, absolute *r* band Sérsic magnitude (truncated at $10 r_e$); rest-frame (*u* – *r*) colour, and; *r* band Sérsic index. In these global parameter spaces, we are able to reproduce several well known morphological relations, including the curved magnitude-radius relation for elliptical galaxies (Graham & Worley 2008; Forbes et al. 2008) and the galaxy population bimodality as has been shown in, e.g., Baldry et al. (2004); Driver et al. (2006); Kelvin et al. (2012).

Using GAMA single-Sérsic (Sérsic 1963, 1968) structural measurements (Kelvin et al. 2012), we maintain that the most meaningful measurement of the total flux of a galaxy is that given by the Sérsic magnitude, truncated at 10 multiples of the half-light radius. This estimate of total flux allows us to derive luminosity functions for both the global population and the constituent morphology sub-populations in each passband (*ugrizYJHK*). We confirm that the total galaxy luminosity function (GLF) is best described by a double-Schechter form (Schechter 1976) with a single distinctive ‘knee’ (L^*/M^*) parameter. Conversely, we find the constituent morphological-type luminosity functions (MLFs) are well described by a single-Schechter form. Tables 3 to 9 provide full Schechter fit parameters for these data across all 9 wavelengths.

Our morphological classifications allow for the division of the cosmic spectral energy distribution (CSED) by morphological type. The CSED describes the instantaneous energy production rate of the Universe, providing a means by which cosmological model predictions of the total local en-

ergy budget may be tested. Here we provide estimates of the CSED by directly summing the flux in our volume limited sample for each morphological type across each wavelength. Note that we include flux measurements from the *FUV* and *NUV* in order to account for the significant energy contribution at wavelengths below 400 nm. The energy production budget today is mainly comprised of both stellar nucleosynthesis and dust reprocessing. Therefore, we have measured both the attenuated (i.e., as observed) and unattenuated (i.e., dust corrected) CSEDs for each morphological type by fitting a series of single stellar population PEGASE models (Fioc & Rocca-Volmerange 1999) to each population.

Based on our dust corrected *FUV* flux estimates, we also construct estimates of the local ($z \sim 0.04$) star formation rate (SFR) density subdivided by morphology. We find the SFR density across this redshift range to be dominated by the intermediate S(B)ab-S(B)cd morphological type systems, declining sharply at earlier or later Hubble types, and confirming the trend seen in James et al. (2008).

In addition, we find that $\sim 58\%$ of the total attenuated (observed) energy output in the local Universe emerges from spheroid dominated galaxies, with the remaining $\sim 42\%$ found in disk dominated systems. The summation of these fits gives a total observed energy output of $(8.53 \pm 0.20) \times 10^{34}$ W Mpc $^{-3}$, in good agreement with that of Driver et al. (2012). The unattenuated CSEDs are derived by applying the photon escape fraction prescription detailed in Driver et al. (2008), calibrated using the radiative transfer models of Popescu et al. (2011), to the S(B)ab-S(B)cd, Sd-Irr and LBS populations only. We find that $\sim 44\%$ of the total unattenuated (corrected) energy output in the local Universe emerges from spheroid dominated galaxies, with the remaining $\sim 56\%$ found in disk dominated systems. The summation of these fits gives a total corrected energy output in the local Universe of $(1.12 \pm 0.15) \times 10^{35}$ W Mpc $^{-3}$.

ACKNOWLEDGEMENTS

This work was supported by the Austrian Science Foundation FWF under grant P23946. AWG was supported under the Australian Research Council's funding scheme FT110100263. GAMA is a joint European-Australasian project based around a spectroscopic campaign using the Anglo-Australian Telescope. The GAMA input catalogue is based on data taken from the Sloan Digital Sky Survey and the UKIRT Infrared Deep Sky Survey. Complementary imaging of the GAMA regions is being obtained by a number of independent survey programs including GALEX MIS, VST KiDS, VISTA VIKING, WISE, Herschel-ATLAS, GMRT and ASKAP providing UV to radio coverage. GAMA is funded by the STFC (UK), the ARC (Australia), the AAO, and the participating institutions. The GAMA website is <http://www.gama-survey.org/>.

References

Abazajian K. N. et al., 2009, *ApJS*, 182, 543
 Agius N. K. et al., 2013, *MNRAS*, 431, 1929
 Allen P. D., Driver S. P., Graham A. W., Cameron E., Liske J., de Propriis R., 2006, *MNRAS*, 371, 2

Arp H., 1965, *ApJ*, 142, 402
 Baldry I. K. et al., 2012, *MNRAS*, 421, 621
 Baldry I. K., Glazebrook K., Brinkmann J., Ivezić Ž., Lupton R. H., Nichol R. C., Szalay A. S., 2004, *ApJ*, 600, 681
 Baldry I. K. et al., 2010, *MNRAS*, 404, 86
 Bamford S. P. et al., 2009, *MNRAS*, 393, 1324
 Bauer A. E. et al., 2013, *MNRAS*, 434, 209
 Benson A. J., Džanović D., Frenk C. S., Sharples R., 2007, *MNRAS*, 379, 841
 Bertin E., 2011, in *Astronomical Society of the Pacific Conference Series*, Vol. 442, *Astronomical Data Analysis Software and Systems XX*, Evans I. N., Accomazzi A., Mink D. J., Rots A. H., eds., p. 435
 Bertin E., Arnouts S., 1996, *A&AS*, 117, 393
 Binggeli B., Sandage A., Tarengchi M., 1984, *AJ*, 89, 64
 Blanton M. R. et al., 2003, *ApJ*, 592, 819
 Brough S. et al., 2011, *MNRAS*, 413, 1236
 Cameron E., 2011, *PASA*, 28, 128
 Caon N., Capaccioli M., D'Onofrio M., 1993, *MNRAS*, 265, 1013
 Caon N., Capaccioli M., D'Onofrio M., 1994, *A&AS*, 106, 199
 Caon N., Capaccioli M., Rampazzo R., 1990, *A&AS*, 86, 429
 Capaccioli M., 1989, in *World of Galaxies (Le Monde des Galaxies)*, Corwin Jr. H. G., Bottinelli L., eds., pp. 208–227
 Cappellari M. et al., 2011, *MNRAS*, 413, 813
 Carollo C. M. et al., 2013, *ApJ*, 773, 112
 Carter D., 1978, *MNRAS*, 182, 797
 Carter D., 1987, *ApJ*, 312, 514
 Ciotti L., 1991, *A&A*, 249, 99
 Conselice C. J., 2006, *MNRAS*, 373, 1389
 Davies R. L., Efstathiou G., Fall S. M., Illingworth G., Schechter P. L., 1983, *ApJ*, 266, 41
 de Vaucouleurs G., 1948, *Annales d'Astrophysique*, 11, 247
 Debattista V. P., Mayer L., Carollo C. M., Moore B., Wadsley J., Quinn T., 2006, *ApJ*, 645, 209
 Diaferio A., Kauffmann G., Balogh M. L., White S. D. M., Schade D., Ellingson E., 2001, *MNRAS*, 323, 999
 Domínguez A. et al., 2011, *MNRAS*, 410, 2556
 Dressler A., 1980, *ApJ*, 236, 351
 Driver S. P., 1999, *ApJ*, 526, L69
 Driver S. P. et al., 2006, *MNRAS*, 368, 414
 Driver S. P. et al., 2011, *MNRAS*, 413, 971
 Driver S. P., Liske J., Cross N. J. G., De Propriis R., Allen P. D., 2005, *MNRAS*, 360, 81
 Driver S. P. et al., 2009, *Astronomy and Geophysics*, 50, 050000
 Driver S. P., Popescu C. C., Tuffs R. J., Graham A. W., Liske J., Baldry I., 2008, *ApJ*, 678, L101
 Driver S. P., Popescu C. C., Tuffs R. J., Liske J., Graham A. W., Allen P. D., de Propriis R., 2007, *MNRAS*, 379, 1022
 Driver S. P., Robotham A. S. G., Bland-Hawthorn J., Brown M., Hopkins A., Liske J., Phillipps S., Wilkins S., 2013, *MNRAS*, 430, 2622
 Driver S. P. et al., 2012, *MNRAS*, 427, 3244
 Drory N., Fisher D. B., 2007, *ApJ*, 664, 640
 Erwin P., Beltrán J. C. V., Graham A. W., Beckman J. E., 2003, *ApJ*, 597, 929

- Fioc M., Rocca-Volmerange B., 1999, arXiv:astro-ph/9912179
- Forbes D. A., Lasky P., Graham A. W., Spitler L., 2008, MNRAS, 389, 1924
- Gadotti D. A., 2009, MNRAS, 393, 1531
- Graham A. W., 2013, Planets, Stars and Stellar Systems, Oswalt T. D., Keel W. C., eds., Vol. 6. Springer Netherlands, Dordrecht
- Graham A. W., Driver S. P., 2005, PASA, 22, 118
- Graham A. W., Driver S. P., Petrosian V., Conselice C. J., Bershadsky M. A., Crawford S. M., Goto T., 2005, AJ, 130, 1535
- Graham A. W., Worley C. C., 2008, MNRAS, 388, 1708
- Gunn J. E., Gott, III J. R., 1972, ApJ, 176, 1
- Guzman R., Gallego J., Koo D. C., Phillips A. C., Lowenthal J. D., Faber S. M., Illingworth G. D., Vogt N. P., 1997, ApJ, 489, 559
- Hill D. T., Driver S. P., Cameron E., Cross N., Liske J., Robotham A., 2010, MNRAS, 404, 1215
- Hill D. T. et al., 2011, MNRAS, 412, 765
- Holmberg E., 1958, Meddelanden fran Lunds Astronomiska Observatorium Serie II, 136, 1
- Hopkins A. M., Beacom J. F., 2006, ApJ, 651, 142
- Hopkins A. M. et al., 2013, MNRAS, 430, 2047
- Hubble E. P., 1926, ApJ, 64, 321
- Hubble E. P., 1936, Realm of the Nebulae
- James P. A., Knapen J. H., Shane N. S., Baldry I. K., de Jong R. S., 2008, A&A, 482, 507
- Jeans J. H., 1919, Problems of cosmogony and stellar dynamics
- Kauffmann G., White S. D. M., Guiderdoni B., 1993, MNRAS, 264, 201
- Kelvin L. S. et al., 2012, MNRAS, 421, 1007
- Kennicutt, Jr. R. C., 1989, ApJ, 344, 685
- Kormendy J., Bender R., 1996, ApJ, 464, L119
- Kormendy J., Bender R., 2012, ApJS, 198, 2
- Larson R. B., Tinsley B. M., Caldwell C. N., 1980, ApJ, 237, 692
- Laurikainen E., Salo H., Buta R., Knapen J. H., Comerón S., 2010, MNRAS, 405, 1089
- Lawrence A. et al., 2007, MNRAS, 379, 1599
- Lintott C. et al., 2011, MNRAS, 410, 166
- Lintott C. J. et al., 2008, MNRAS, 389, 1179
- Liske J., Lemon D. J., Driver S. P., Cross N. J. G., Couch W. J., 2003, MNRAS, 344, 307
- Loveday J. et al., 2012, MNRAS, 420, 1239
- Misgeld I., Hilker M., 2011, MNRAS, 414, 3699
- Montero-Dorta A. D., Prada F., 2009, MNRAS, 399, 1106
- Moore B., Katz N., Lake G., Dressler A., Oemler A., 1996, Nature, 379, 613
- Nair P. B., Abraham R. G., 2010, ApJS, 186, 427
- Navarro J. F., Benz W., 1991, ApJ, 380, 320
- Park C., Gott, III J. R., Choi Y.-Y., 2008, ApJ, 674, 784
- Pastrav B. A., Popescu C. C., Tuffs R. J., Sansom A. E., 2013a, A&A, 553, A80
- Pastrav B. A., Popescu C. C., Tuffs R. J., Sansom A. E., 2013b, A&A, 557, A137
- Peng C. Y., Ho L. C., Impey C. D., Rix H.-W., 2010, AJ, 139, 2097
- Phillipps S., Driver S., 1995, MNRAS, 274, 832
- Pimblet K. A., Jensen P. C., 2012, MNRAS, 426, 1632
- Popescu C. C., Misiriotis A., Kylafis N. D., Tuffs R. J., Fischera J., 2000, A&A, 362, 138
- Popescu C. C., Tuffs R. J., Dopita M. A., Fischera J., Kylafis N. D., Madore B. F., 2011, A&A, 527, A109
- Popesso P., Biviano A., Böhringer H., Romaniello M., 2006, A&A, 445, 29
- Prescott M., Baldry I. K., James P. A., 2009, MNRAS, 397, 90
- Reynolds J. H., 1920, MNRAS, 80, 746
- Robotham A. et al., 2010, PASA, 27, 76
- Robotham A. S. G., Driver S. P., 2011, MNRAS, 413, 2570
- Robotham A. S. G. et al., 2011, MNRAS, 416, 2640
- Rowlands K. et al., 2012, MNRAS, 419, 2545
- Saha K., Martinez-Valpuesta I., Gerhard O., 2012, MNRAS, 421, 333
- Salpeter E. E., 1955, ApJ, 121, 161
- Sandage A., 1961, The Hubble atlas of galaxies
- Sandage A., Binggeli B., 1984, AJ, 89, 919
- Schechter P., 1976, ApJ, 203, 297
- Sérsic J. L., 1963, Boletín de la Asociacion Argentina de Astronomia La Plata Argentina, 6, 41
- Sérsic J. L., 1968, Atlas de galaxias australes
- Shapley H., 1938, Nature, 142, 715
- Shapley H., Paraskevopoulos J. S., 1940, Proceedings of the National Academy of Science, 26, 31
- Simard L., Mendel J. T., Patton D. R., Ellison S. L., McConnell A. W., 2011, ApJS, 196, 11
- Somerville R. S., Gilmore R. C., Primack J. R., Domínguez A., 2012, MNRAS, 423, 1992
- Steinmetz M., Navarro J. F., 2002, New A, 7, 155
- Stinson G. S., Dalcanton J. J., Quinn T., Kaufmann T., Wadsley J., 2007, ApJ, 667, 170
- Stoughton C. et al., 2002, AJ, 123, 485
- Taylor E. N. et al., 2011, MNRAS, 418, 1587
- Tuffs R. J., Popescu C. C., Völk H. J., Kylafis N. D., Dopita M. A., 2004, A&A, 419, 821
- van den Bergh S., 1976, ApJ, 206, 883
- van der Wel A., 2008, ApJ, 675, L13
- Wilman D. J., Erwin P., 2012, ApJ, 746, 160
- York D. G. et al., 2000, AJ, 120, 1579

APPENDIX A: REDSHIFT LIMITS

Based on prior measurements of structural properties as presented in Allen et al. (2006) and Simard et al. (2011), we calculate the typical physical sizes of bulges and disks in the local Universe. Adopting the redshifts provided in each respective catalogue, we convert their reported bulge and disk angular sizes to physical sizes (in kpc) in accordance with our preferred cosmology, namely: $(H_0, \Omega_m, \Omega_\Lambda) = (70 \text{ km s}^{-1} \text{ Mpc}^{-1}, 0.3, 0.7)$. An appropriate conversion between exponential disk scalelength (as provided in both catalogues) and half-light radius is achieved using the well known relation

$$r_e = b^n h \quad (\text{A1})$$

where h is the disk scalelength, n is the Sérsic index (a measure of the shape of the galaxy light profile; see Section 2.1.1 for further details) and b is a function of n . For $n = 1$, $b^n = 1.678$. We discard those model fits that lie outwith the range $0.1 < B/T < 0.9$, limiting each catalogue to those systems that are not dominated by the flux from a single

component. Allen et al. (2006) model fits are to *B*-band imaging data, whereas Simard et al. (2011) fits are in the SDSS *r*-band. As shown in Kelvin et al. (2012), one expects a variation in observed half-light radii with wavelength. The best fitting relations for both spheroidal (bulge) and disk components are given by:

$$\log r_{\text{e,sph}} = -0.304 \log \lambda_{\text{rest}} + 1.506 \quad (\text{A2})$$

$$\log r_{\text{e,disk}} = -0.189 \log \lambda_{\text{rest}} + 1.176 \quad (\text{A3})$$

where λ_{rest} is the rest-frame wavelength. Accordingly, we correct the Allen et al. (2006) half-light radii from *B*-band (445 nm) to the *r*-band (622 nm). We match both catalogues to the GAMA-I tiling catalogue (version 16) to limit our analyses to galaxies that lie within the GAMA volume, and calculate 3-sigma-clipped robust mean values for the bulge and disk components in both studies.

We find the typical sizes for bulge components in the local Universe as measured in the *r*-band to be 1.93 ± 1.20 kpc and 3.02 ± 1.65 kpc for Allen and Simard, respectively. We find the typical sizes for the corresponding disk components to be 8.19 ± 3.62 kpc and 8.41 ± 4.45 kpc, for Allen and Simard, respectively¹¹. Figure A1 shows the apparent angular size for structures of these physical sizes at varying redshift. The red (blue) solid (dashed) line represents the apparent angular size for bulges (disks) in the Allen (Simard) data, as indicated. The shaded semi-transparent regions around each line represents the half-sigma scatter in the data. In addition, the horizontal dotted line lies at an angular size of $1.1''$, which corresponds to the typical *r*-band seeing in SDSS (Kelvin et al. 2012).

For this study, we define an upper redshift limit of $z = 0.06$. This limit is chosen such that the majority of bulges (the limiting structural component) should remain resolvable. A lower limit of $z = 0.025$ is also adopted to avoid low galaxy number densities below this redshift and to ensure that measured redshifts are not dominated by peculiar velocities.

APPENDIX B: COMPARISON WITH GALAXY ZOO MORPHOLOGIES

To test our visual classifications we compare our morphological classifications to those of the well-established citizen science project Galaxy Zoo (Lintott et al. 2008). We employ the Galaxy Zoo 1 data release (GZ1; Lintott et al. 2011, Table 2) in our analysis below.

GZ1 contains 667,944 sources down to an SDSS apparent magnitude limit of $r = 17.77$ mag for all galaxies

¹¹ Although it is crucial for us to estimate the typical *observed* sizes of bulges and disks in the local Universe when defining appropriate sample redshift limits, we note that due to the effects of dust, projection effects and bulge/disk decomposition considerations, the measured sizes differ from the intrinsic underlying ones. Using the corrections from Pastrav et al. (2013a,b) for $\tau_B^f = 3.8$ (the same average dust opacity used to correct for dust attenuation), we obtain average intrinsic bulge sizes of 1.80 kpc and 2.82 kpc for the Allen and Simard samples, respectively, with corresponding intrinsic disk sizes of 7.00 kpc and 6.19 kpc.

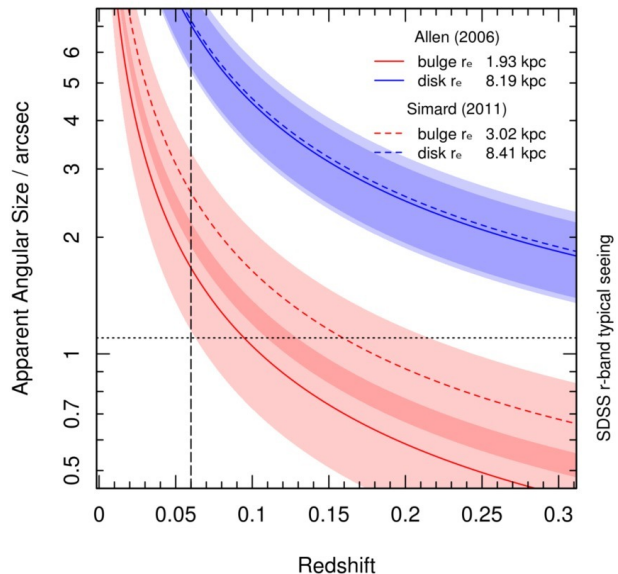


Figure A1. Apparent angular size for typical bulges and disks at varying redshifts. The red (blue) solid (dashed) line represents the apparent angular size for bulges (disks) in the Allen (Simard) data, as indicated. The shaded semi-transparent regions around each line represents the half-sigma scatter in the data. In addition, the horizontal dotted line lies at an angular size of $1.1''$, which corresponds to the typical *r*-band seeing in SDSS (Kelvin et al. 2012). Our chosen upper redshift limit of $z = 0.06$ is shown as a vertical dashed line.

in the SDSS Data Release 7 which have spectra included. Of these 667,944 objects, 1,779 galaxies exhibit a direct match with the galaxies in our volume limited GAMAnear sample of 3,727 ($\sim 48\%$) when matching by SDSS object ID (OBJID). Each galaxy in the Galaxy Zoo catalogue is classified as either ‘elliptical’, ‘spiral’ or ‘uncertain’, with an associated probability. We adopt a probability threshold of 80%. A markedly high fraction of this subset is classified by Galaxy Zoo as ‘uncertain’ (1,050; 59.0%), with the remainder as ‘elliptical’ (143; 8.0%) and ‘spiral’ (586; 32.9%). For comparison, our own matched sub-sample is similarly split into three comparable classification bins: elliptical (324; 18.2%), spiral¹² (S0-Sa→Sd-Irr, 1416; 79.6%) and LBS/star (39; 2.2%).

Figure B1 shows the cross-correlation results between our own visual classifications and those provided by Galaxy Zoo. The number of galaxies within each bin are shown as ‘correlation bubbles’, with larger bubbles corresponding to a higher fraction of objects within that bin. The fraction of galaxies within each classification bin is quantified as a percentage of galaxies in our own study (left) and of galaxies from Galaxy Zoo (right). As is shown, the vast majority (99.8%) of the Galaxy Zoo spiral population are also classified as spirals by our method (i.e., the Galaxy Zoo spiral population is essentially a subset of our own), but not all

¹² Although lenticular and irregular types exist within this combined population, we label it ‘spiral’ for brevity and ease of comparison to the Galaxy Zoo data.

of our spiral galaxies are found to be spiral in the Galaxy Zoo data. A similarly large fraction of the Galaxy Zoo elliptical population (79.7%) are also classified as elliptical by our method, with approximately one fifth of Galaxy Zoo ellipticals classified as spirals in this study. The majority of Galaxy Zoo uncertain galaxies are classified as spiral by our method (76.4%), which may be expected owing to the typically fainter surface brightnesses of galaxies of this type. As is shown in the left panel, more than half of each grouping fall within the Galaxy Zoo uncertain class, almost accounting for the entirety of our LBS/star population. This large Galaxy Zoo uncertain population no doubt arises due to the stringent 80% classification criterion recommended for use in Lintott et al. (2011). We note that the application of a lower 66% threshold (in line with our own classification method) forces a significant fraction of the uncertain population into the two standard ‘elliptical’ and ‘spiral’ sub-populations, in good agreement with our own results, albeit with a larger margin of error. Despite the large fraction of uncertain galaxies, we opt to maintain the recommended classification criterion of 80% for our analyses. If one removes the uncertain grouping from this figure, we find that the primary axis (i.e., the [Elliptical, Elliptical] \rightarrow [Spiral, Spiral] axis) remains strong when using either our own method or Galaxy Zoo as a reference baseline, indicating a good level of agreement between our own classifications and those of Galaxy Zoo.

To summarise, while we acknowledge that Galaxy Zoo morphologies are preferred for studies that require robust morphological information for a large ($> 10^5$) number of systems, we advocate that detailed visual inspection by a team of experts produces notable advantages over Galaxy Zoo for small datasets such as that presented in this study. The creation of our own classification schema has allowed us full control over, for example: classification criteria (and therefore the ultimate resolution on available Hubble types); postage stamp image creation, including red-green-blue filter selection, image sizes and image scaling (both logarithmic and arctan), and, significantly; our final sample selection. As shown in Figure B1, we find a good level of agreement in morphological type between those galaxies that exist in both the Galaxy Zoo dataset and our own GAMAnear sample. This confirms that our classification schema is robust and equally applicable to those additional galaxies in our sample that do not have a counterpart in the Galaxy Zoo database.

APPENDIX C: MORPHOLOGIES IN COLOUR-INDEX SPACE

Below we provide postage stamp examples of each morphological type as defined in Figure 3. These types are: Little Blue Spheroids (LBS), Figure C1; ellipticals, Figure C2; lenticular/early-type spirals, Figure C3; barred lenticular/early-type spirals, Figure C4; late-type spirals, Figure C5; barred late-type spirals, Figure C6, and; disk-dominated spirals, Figure C7. Each figure is arranged according to the global K band Sérsic index and rest-frame $u-r$ colour of the galaxy. Postage stamp images are created from RGB=*Hig* input data and are approximately $40'' \times 40''$ in size.

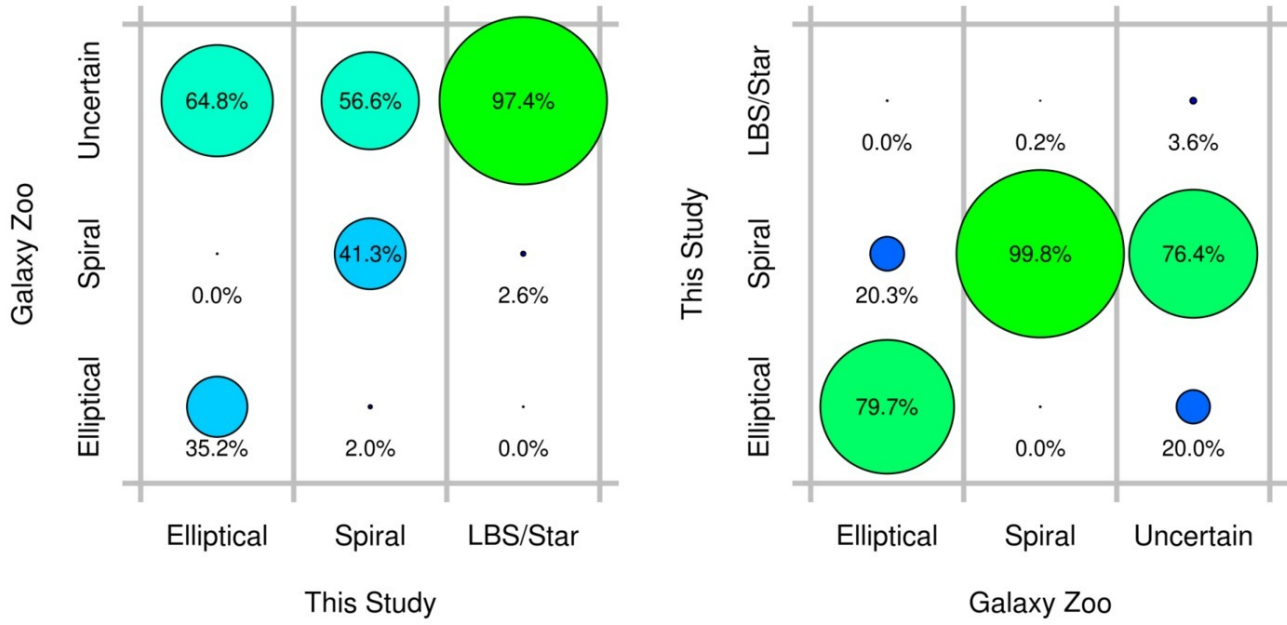


Figure B1. A visual representation of the level of agreement between our visual classifications and those provided by the Galaxy Zoo project (Lintott et al. 2008, 2011). These figures are constructed using a common matched dataset of 1,779 galaxies from GAMAnear and Table 2 of Lintott et al. (2011). Percentages shown depict the fractional agreement with our own classifications (left) and with the Galaxy Zoo classifications (right), that is; percentages in any given column total 100%.

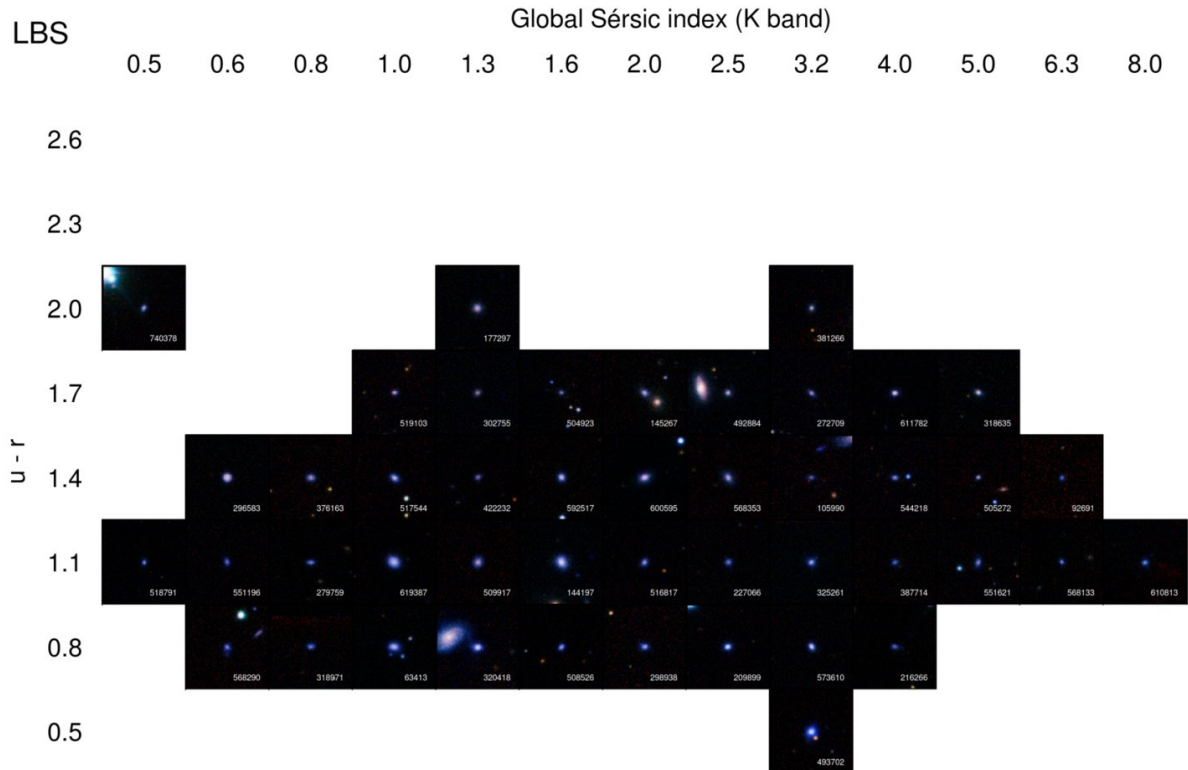


Figure C1. Little Blue Spheroids in $u - r$ colour-Sérsic index space.

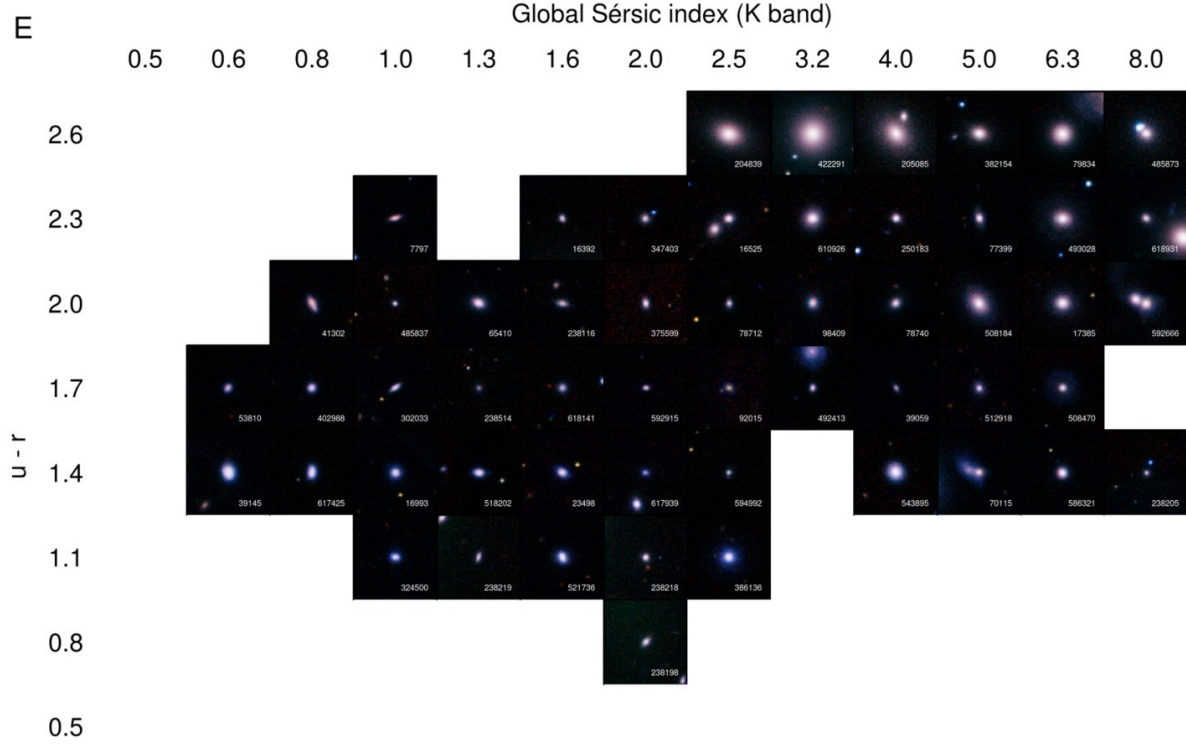


Figure C2. As Figure C1, but for ellipticals.

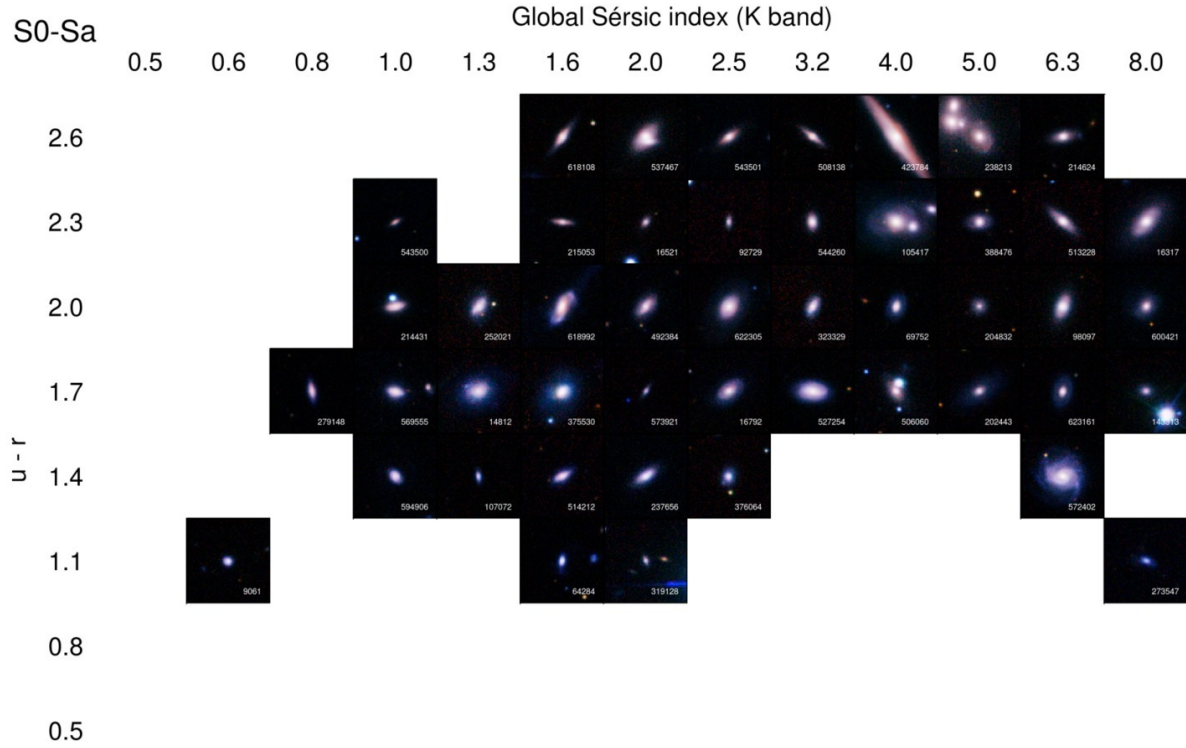


Figure C3. As Figure C1, but for S0-Sa type galaxies.

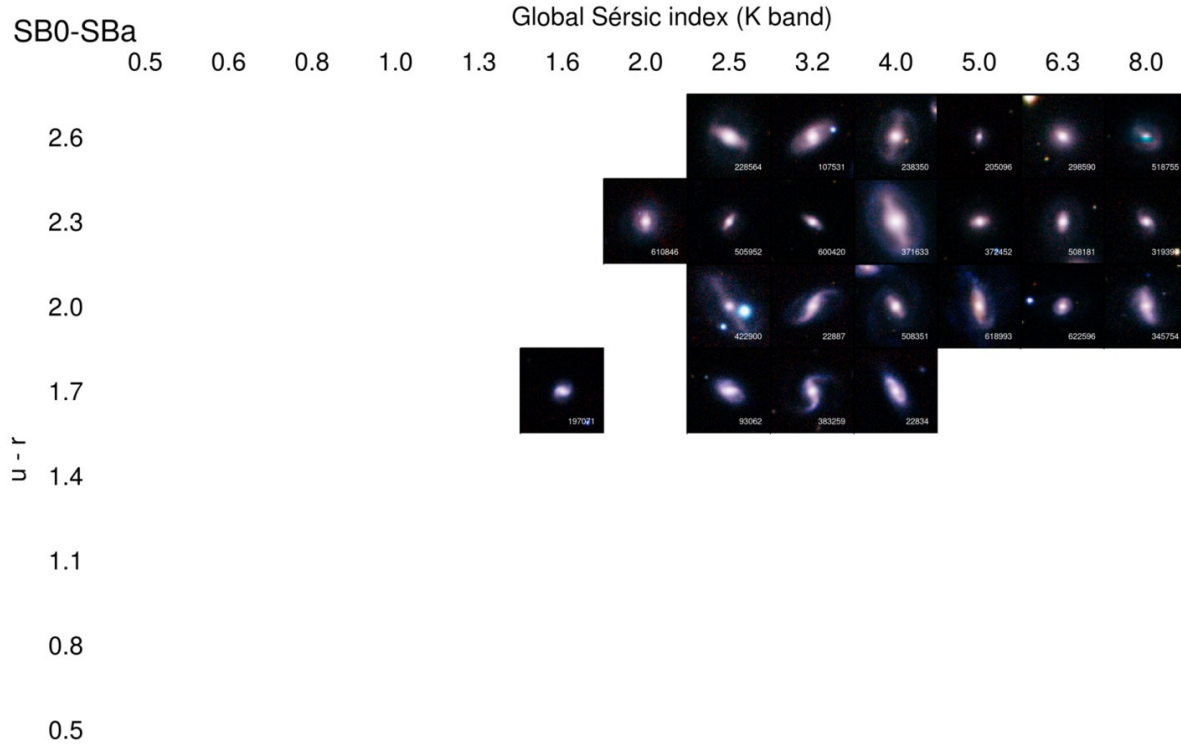


Figure C4. As Figure C1, but for SB0-SBa type galaxies.

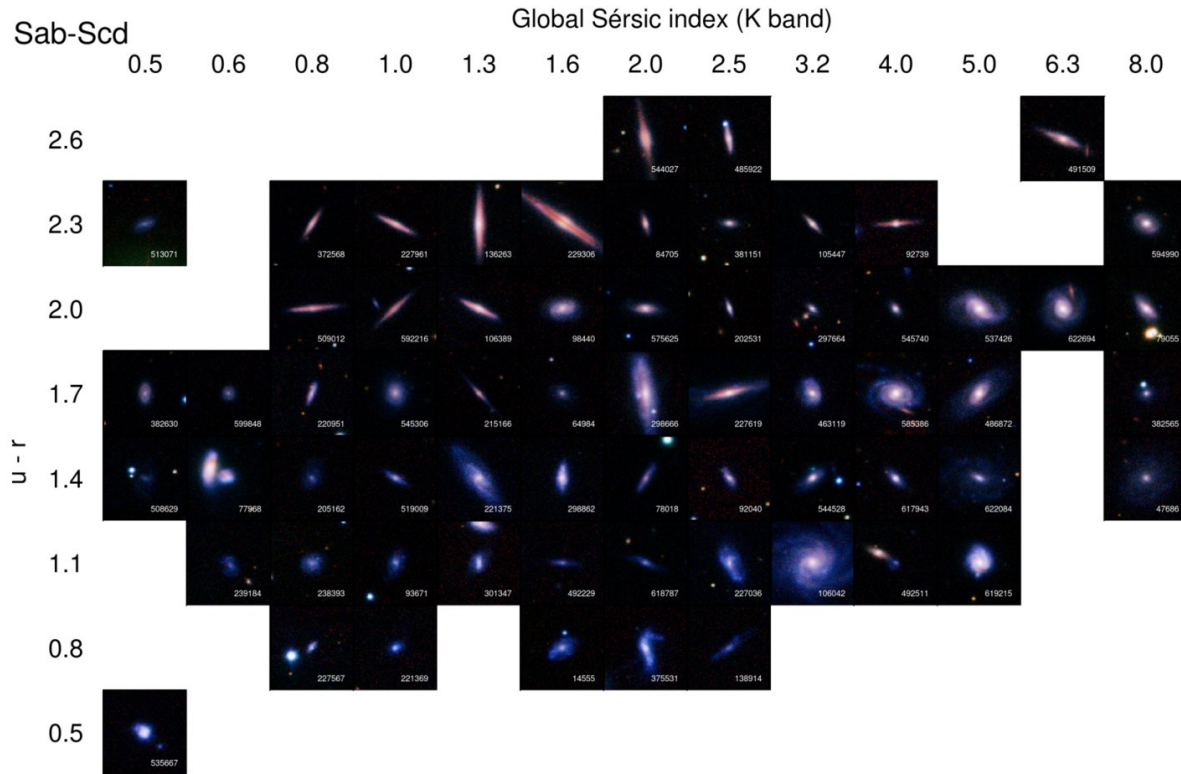


Figure C5. As Figure C1, but for Sab-Scd type galaxies.

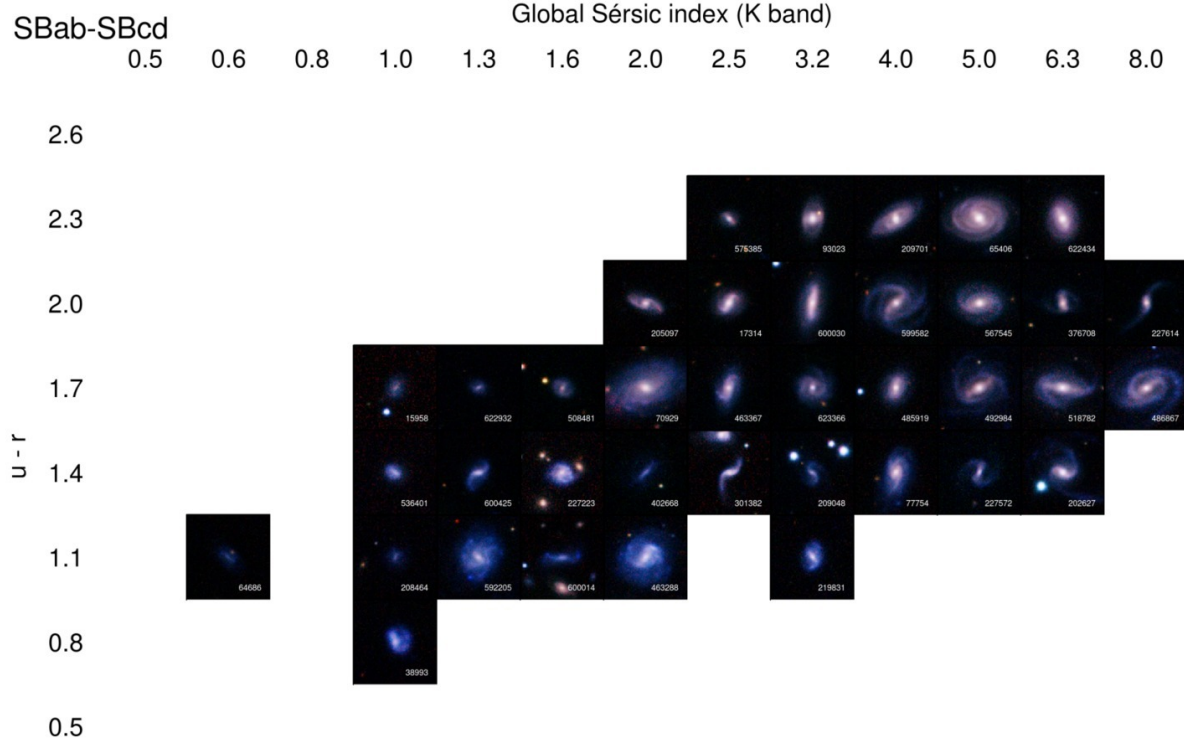


Figure C6. As Figure C1, but for SBab-SBcd type galaxies.

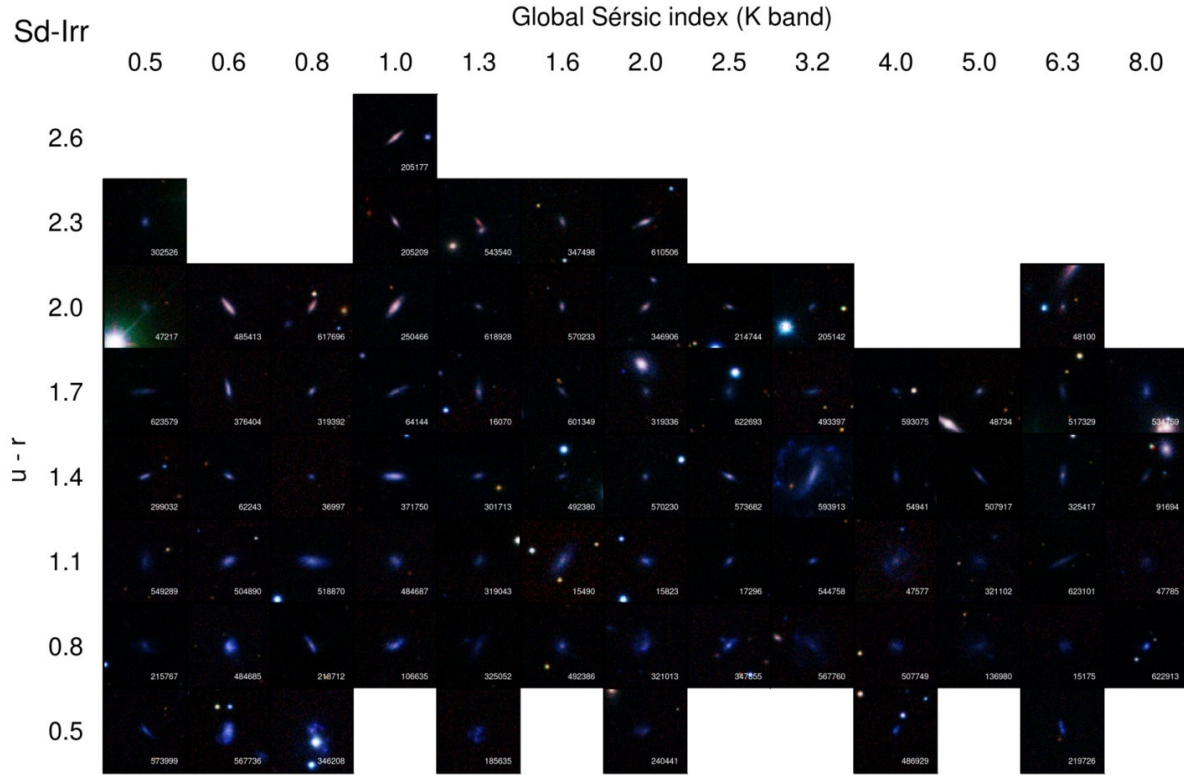


Figure C7. As Figure C1, but for Sd-Irr type galaxies.